Univerzita Karlova v Praze
Matematicko-fyzikální fakulta

Diplomová práce

2008 Silvie Mašková

Charles University, Prague
Faculty of Mathematics and Physics

DIPLOMA THESIS

Silvie Mašková

Hydrides of uranium intermetallics

Department of Condensed Matter Physics

Supervisor: Doc. RNDr. Ladislav Havela, CSc.

2008

Acknowledgements

At the very beginning I would like to thank all the people who contributed to the realization of the following work.

First of all I should express my sincerest gratitude to my supervisor Doc. RNDr. Ladislav Havela, CSc. whose thorough guidance led me through the whole process of the research activity – from the stage of stating the task till the search for the methods of realization and the analysis. Thanks to his huge experience, keen observations, understandable explanations, patience and discussions I could gradually progress in my own understanding and skills.

My thanks go to RNDr. Stanislav Daniš, Ph.D., whose skills in crystal structure analysis helped to solve different non-trivial tasks.

I want to express my deep gratitude to RNDr. Eva Šantavá, CSc. for her kind assistance in the physical properties measurements at the Joint Laboratory for Magnetic Studies.

Last but not least I want to thank my family and friends for their love, support, and encouragement.

Prohlašuji, že jsem svou diplomovou práci napsala samostatně a výhradně s využitím citovaných pramenů. Souhlasím se zapůjčováním práce.

V Praze dne 18.04.2008 Silvie Mašková

Contents:

Název práce: Hydridy intermetalických sloučenin uranu

Autor: Silvie Mašková

Katedra: Katedra fyziky kondenzovaných látek

Vedoucí diplomové práce: Doc. RNDr. Ladislav Havela, CSc.

e – mail vedoucího: havela@mag.mff.cuni.cz

Abstrakt: Studovali jsme změny magnetických vlastností vlivem hydrogenace u UTX sloučenin, které dokazují, že dopování U intermetalik intersticiálním vodíkem vede ke zvýraznění magnetických vlastností. Naopak jakékoli ředění uranové podmříže nemagnetickým prvkem vede k potlačení magnetismu. Jak bylo zjištěno např. u $U_{1-x}Th_xCoSn$, kdy uspořádání na dlouhou vzdálenost zaniká kolem 60% Th. Všechny sloučeniny této série krystalizují v hexagonální struktuře typu ZrNiAl, prostorová grupa $P\overline{6}2m$. Je zajímavé studovat, jestli se interakce s H mění při substituci uranu thoriem a jestli jsou magnetické vlastnosti ovlivněny dopováním H stejně jako u UCoSn, kde vede ke zvýšení T_C z 82 K na 102 K pro $UCoSnH_{1.4}$. V práci jsou prezentovány změny krystalové struktury a magnetických vlastností vlivem hydrogenace u $U_{1-x}Th_xCoSn$ (x = 0.2, 0.4, 0.6, 0.8, 1).

Klíčová slova: uranové sloučeniny, magnetické vlastnosti, absorpce vodíku

Title: Hydrides of uranium intermetallics

Author: Silvie Mašková

Department: Department of Condensed Matter Physics

Supervisor: Doc. RNDr. Ladislav Havela, CSc.

Supervisor´s e-mail address: havela@mag.mff.cuni.cz

Abstract: We have been studying variations of magnetic properties as a function of hydrogen concentration for large families of UTX compounds, which prove that doping of U intermetallics by interstitial hydrogen leads to stronger magnetic properties. On the other hand, any dilution of uranium sublattice by a non-magnetic element leads to the suppression of magnetism. This was demonstrated e.g. on the case of $U_{1-x}Th_xCoSn$, in which the long-range ferromagnetism vanishes at approx. 60% Th, preserving the same hexagonal structure (ZrNiAl type, space group $P\overline{6}2m$) through the whole concentration range. It is intriguing to investigate whether the interaction with H is changed when replacing Th for U, and whether magnetic properties are affected by the H doping in the analogous way as in pure UCoSn, in which it leads to the increase of T_C from 82 K to 102 K for $UCoSnH_{1.4}$. Here we report on the changes of crystal structure and magnetic properties due to hydrogenation of $U_{1-x}Th_xCoSn$ (x = 0.2, 0.4, 0.6, 0.8, 1).

Keywords: uranium compounds, magnetic properties, hydrogen absorption

1. Introduction

Interstitial doping by hydrogen is a powerful tool capable of changing both crystal and electronic structure of intermetallic compounds. As a result, the new compounds (hydrides) exhibit qualitatively new physical properties and such modifications provide us with additional information on the peculiarities of interatomic interactions in the initial compounds. One should consider two main effects of hydrogen absorption on intermetallic compounds. Hydrogen plays the role of a negative pressure agent (acts as small perturbation on the system expanding it). The other sometimes more important effect is the bonding of hydrogen to other atoms in the lattice.

Intermetallic compounds of 5*f* elements, including uranium, are especially sensitive to hydrogen absorption. For purely band systems, the interatomic distance between the uranium atoms is a crucial parameter, which determines the magnetic properties. However, most of uranium intermetallics are characterized by a 5*f*-ligand hybridization, and the strength of hybridization is an extremely important parameter. Hydrogen intrusion can easily modify the hybridized band by withdrawing electronic states due to chemical bonding with the atoms, which contribute to the band.

We have been studying variations of magnetic properties as a function of hydrogen concentration for large families of UTX compounds (T - transition metal, X – p-metal), which prove that doping of U intermetallics by interstitial hydrogen leads to stronger magnetic properties. On the other hand, any dilution of uranium sublattice by a non-magnetic element leads to the suppression of magnetism. It is intriguing to investigate whether the interaction with H is changed when replacing Th for U, and whether magnetic properties are affected by the H doping in the analogous way as in pure UCoSn, in which it leads to the increase of T_C from 82 K to 102 K for $UCoSnH_{1.4}$.

This work presents the results of studies of changes of crystal structure and magnetic properties due to hydrogenation of $U_{1-x}Th_xCoSn$ (x = 0.2, 0.4, 0.6, 0.8, 1) system.

In addition, the project assumed the study of a SSE (Solid-State Electrotransport) refinement on purity of U metal used as a starting material. This task could not be finalized in a due time. The reason is that a decision was taken to undertake the uranium SSE in a new equipment, which is only to be completed. Therefore this thesis contains only the first part, the characterization of the U metal prior to SSE refinement, by means of magnetic susceptibility, specific heat, and electrical resistivity.

2. Theory

2.1. Solid-state properties of actinides

Elements between actinium ($Z = 89$) and lawrencium ($Z = 103$) are called actinides. Generally they can be described as $\mathrm{Rn}^{86}\ 5f^{N}\ 6d^{1}\ 7s^{2}$ ($N = 0 - 14$). The part of actinides after americium has localized $5f$ electrons. They represent a certain analogy to the rare-earth metals, for which the $4f$ states are localized. On the other hand, actinides before Am do not have well localized $5f$ states.

2.1.1. Ground state properties of localized electron systems

The $4f$ shell responsible for magnetic properties of rare earths has a small radial extent and is also well shielded by $5s$ and $5p$ shells that $4f$ shell remains localized even if rare earth atoms form a compound. This allows treating the $4f$ shell similarly to the atomic shell of free atom. The ground state (characterized by quantum numbers S, L, J) is determined by the Hund's rules, which say that l and s of the individual electrons would combine in such way that:

1. the total spin S is maximized
2. subject to maximum S the total orbital momentum is also maximized
3. in light rare earths L and S combine like $J = L - S$, in heavy rare earths like $J = L + S$.

The magnetic moment in the ground state is given by:

$$\mu = g\frac{e}{2m}J, \tag{1}$$

where g is called Landé factor given by:

$$g = 1 + \frac{J(J+1) + S(S+1) - L(L+1)}{2J(J+1)}. \tag{2}$$

Magnetic ordering arises due to indirect exchange interaction, mediated by polarization of conducting electrons, called RKKY interaction (named after four scientists: Ruderman, Kittel, Kasuya, and Yoshida).

2.1.2. Ground state properties of itinerant electron systems – Stoner model

The Stoner theory [1,2] of itinerant magnetism for *d*-metals is the simplest theory describing magnetic order in band systems. It describes particles, which move freely in the periodic potential of the solid as a more or less free electron gas. The electron states are not described by discrete energy levels but by density of states formed by energy bands. The model is based on the following postulates:

- the carriers of magnetism are the electrons in the *d* (or *f*) band;
- effects of exchange are treated within a molecular field term;
- Fermi statistics should be fulfilled.

The theory is based on a paramagnetic density of states, which is split into two identical bands for spin-up and spin-down. If an external magnetic field (molecular field) is applied, the bands become shifted to new values ε_f^+ for spin-up and ε_f^- for spin-down and two sub-bands are formed due to the redistribution of electrons. The occupancies of the spin-up n^+ and spin-down n^- bands differ therefore. The Stoner equations can be formulated:

$$n^{\pm} = \int_0^{\infty} N(\varepsilon) \frac{1}{\exp(\frac{\varepsilon}{k_B T} - \eta^{\pm}) + 1} d\varepsilon \tag{3}$$

$$k_B T \eta^{\pm} = k_B T \eta \pm \frac{IM}{2} \pm \mu_B H_{ex} \text{ with } \eta = \frac{\mu}{K_B T}$$

μ is chemical potential, which is equal to the Fermi energy what is the energy of the highest occupied state, and consequently the new Fermi energies, caused by the field, can be considered as chemical potentials for spin-up (+) and spin-down (−) as μ^+ and μ^-. The energy shift due to splitting can be given as:

$$\Delta E = IM = I\,(n^+ - n^-) \tag{4}$$

Both in Eqns. (3) and (4), the quantity *I* is the Stoner exchange factor and *M* is the magnetic moment. Magnetic susceptibility is determined therefore as:

$$\chi = \frac{M}{H} = \frac{2\mu_B^2 \int_0^\infty N(\varepsilon) \left| \frac{df}{d\varepsilon} \right| d\varepsilon}{1 - I \int_0^\infty N(\varepsilon) \left| \frac{df}{d\varepsilon} \right| d\varepsilon} \tag{5}$$

where $df/d\varepsilon$ is the energy derivative of the Fermi-Dirac distribution. Eqn. (5) is the most general form of the Stoner susceptibility. At $T = 0$ K it is reduced to:

$$\chi = \frac{2\mu_B^2 N(\varepsilon_F)}{1 - IN(\varepsilon_F)} = 2\mu_B^2 N(\varepsilon_F) S \tag{6}$$

The term $2\mu_B^2 N(\varepsilon_F)$ is the Pauli susceptibility describing non-interacting (no exchange) gas of free electrons and S is Stoner enhancement factor. If the $I^*N(\varepsilon_F)$ product is larger than unity, then χ becomes negative and the formation of spontaneous magnetic order occurs. This gives rise to well-known Stoner criterion, which defines the onset of magnetism if

$$IN(\varepsilon_F) \geq 1 \tag{7}$$

Since Stoner exchange factor I is quasi-atomic property which depends only very little on chemical or metallurgical effects (bonding, alloying, etc.), the possible formation of magnetic moments depends on the density of states at Fermi level $N(\varepsilon_F)$.

2.2. Properties of uranium intermetallic compounds

Magnetic properties of uranium compounds cannot be described by one general theory, since the properties of actinides intermetallics are strongly dependent of the degree of the localization of 5*f* states. Compounds with localized 5*f* states are similar to lanthanides. On the other hand compounds with itinerant 5*f* electrons can be described by the Stoner-Edwards-Wohlfarth theory based on simple ideas in the previous chapter. The degree of localization of uranium compounds is dependent on the inter-uranium spacing. In uranium compounds the critical spacing for Stoner criterion being fulfilled is $d_{\text{U-U}} = 3.4 – 3.6$ Å. This value is called the Hill limit. The ground state of compounds with smaller inter-uranium spacing is typically nonmagnetic (often superconducting). For $d_{\text{U-U}}$ larger than Hill limit they incline to the magnetic ground state.

For compounds with $d_{U\text{-}U}$ larger than the Hill limit, the main control parameter is not the inter-uranium spacing, but the hybridization of the $5f$ states with electronic states of other elements. This is important for the compounds with the transition metals. The $5f$ states of strongly electropositive uranium remain pinned at E_F, whereas the late transition metals, being much more electronegative, have particular d states shifted toward higher binding energies, thus leaving the $5f$–d overlap in energy scale small. The d-metals, which are magnetically ordered in pure state like cobalt, nickel or iron, become in most cases nonmagnetic in uranium compounds. Exceptions are the compounds in which d-magnetism prevails due to a very high content of the transition metal.

We can conclude that magnetic properties of uranium intermetallics are strongly dependent on the peculiarities of crystal structure (inter-uranium distances, atomic environment) and the electronic structure (the degree of f–ligand hybridization, the tendency for localization or itinerancy). Any tiny modifications can lead to huge changes in magnetism. These small modifications can be provided by interstitial doping by hydrogen to study their influence on the compound.

2.3. Hydrides

In the narrowest sense, the term hydride is used just in cases when metal lattice is changed upon hydrogen absorption. However we will use this term in wider sense. We will define hydrides as compounds for which the hydrogen absorption leads to the modifications of the crystal structure, such as pure lattice expansion or the formation of a new structure.

Hydrogen absorption can be used to modify magnetic properties of uranium ternary intermetallics. After interstitial hydrogen doping the crystal lattice can be several percent larger than before hydrogenation.

2.3.1. Binary Diagrams of Metal–Hydrogen systems and Hydride Formation Criteria.

The phase diagrams of metal–hydrogen systems are often rather complicated and contain several ordered structures, especially at lower temperatures. The metal–hydrogen compounds differ essentially from the ordinary alloys formed of solid elements: we cannot change the temperature of a hydride specimen without consequent change of the composition. The exchange of hydrogen between initial compound and the surrounding atmosphere is of crucial importance in treating metal–hydrogen systems. The equilibrium concentration of hydrogen in a specimen is a unique function of the temperature *T* and pressure *p* of the surrounding H_2 gas. On Fig.1, a binary phase diagram Ta–H is presented as an example. This diagram shows the formation of the solid solution of hydrogen in tantalum.

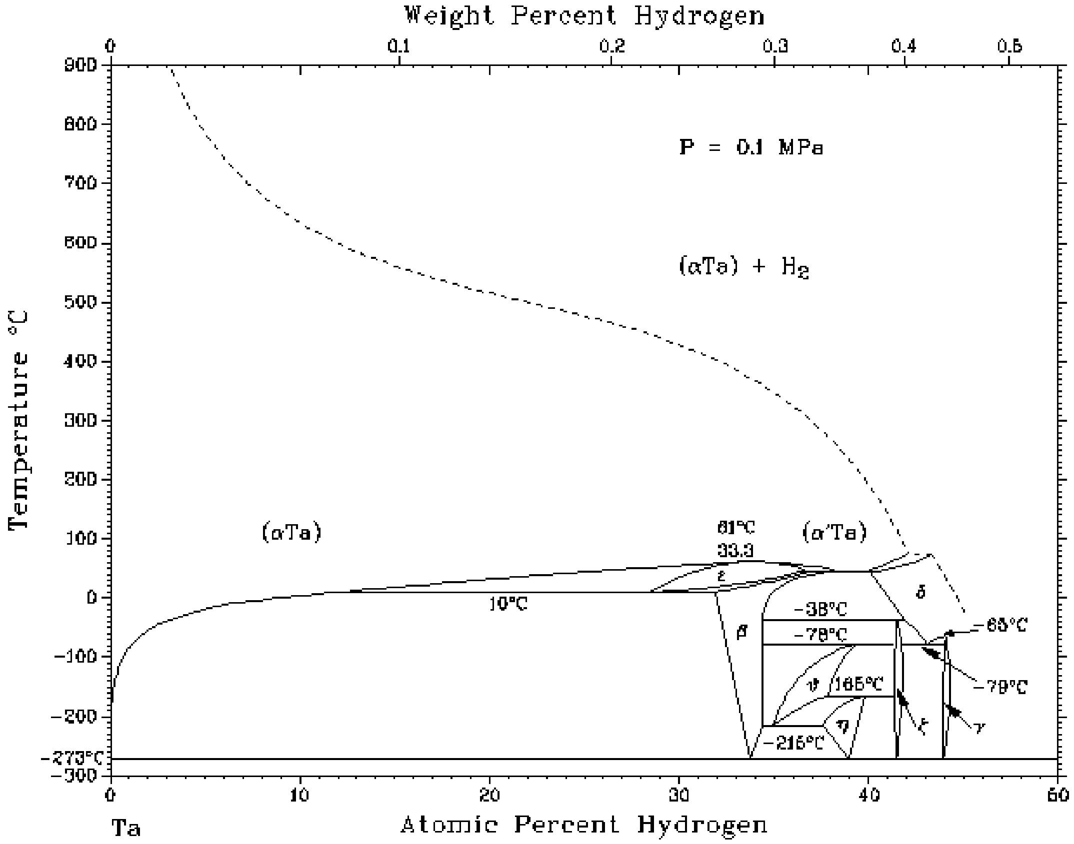

Fig.1: Binary phase diagram of tantalum hydride

In the case of intermetallic hydrides, certain positions for hydrogen atoms are preferred. Fig.2 presents some favorable positions on the example of three principal crystal structures (*fcc*, *hcp*, and *bcc*). Only two types of interstitial sites – octahedral and tetrahedral sites are practically the only ones that are occupied by hydrogen atoms.

In the crystal structure determination of hydrides, X-ray diffraction should be substituted by neutron experiments in order to locate the positions of hydrogen atoms. In most cases it is better to perform neutron diffraction experiments on deuterides because the coherent scattering cross section is much larger and incoherent cross section is much smaller in deuterium than in hydrogen. The site locations of hydrogen and deuterium atoms are mostly (but not necessarily) the same.

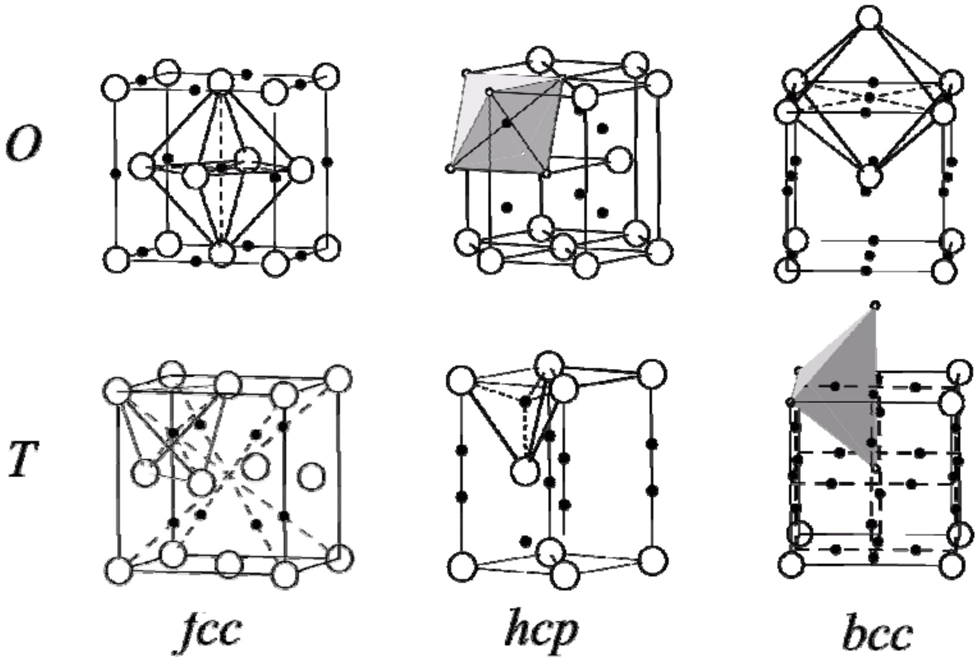

Fig. 2: Interstitial sites (octahedral (*O*) and tetrahedral (*T*)) in face-centered cubic (*fcc*), hexagonal closed-packed (*hcp*) and body-centered cubic (*bcc*) structures. The interstitials are shown as black dots.

Some results of previous investigations of U ternaries [3,4] are shown in the Table 1.

	A (Å)	*c* (Å)	*V* ($Å^3$)	d_{U-U} (Å)	$\Delta V/V$ (%)	T_C (K)	T_N (K)
UCoSn	7.1459	3.9943	176.6	3.74	-	82	-
$UCoSnH_{1.4}$	7.2386	4.0189	182.4	3.78	3.3	102	-
URuSn	7.3509	3.9496	184.8	3.84	-	54	-
$URuSnH_{1.4}$	7.3932	3.9492	186.9	3.87	1.1	51	-
UNiAl	-	-	-	-	-	-	19
$UNiAlH_{2.3}$	-	-	-	-	-	-	99
UPdSi	-	-	-	-	-	-	31
$UPdSiH_{2.0}$	-	-	-	-	-	-	46
UNiSi	-	-	-	-	-	-	85
$UNiSiH_{2.0}$	-	-	-	-	-	98	-
U_2Ni_2In	7.390	3.576	195.3	3.58	-	-	14
$U_2Ni_2InH_{1.9}$	7.547	3.662	208.6	3.66	6.8	-	60
U_2Ni_2Sn	7.236	3.695	194.9	3.56	-	-	26
$U_2Ni_2SnH_{1.8}$	7.445	3.764	208.6	3.73	6.8	-	84

Table. 1: Changes of parameters of some intermetallics caused by hydrogenation: lattice parameters *a* and *c*, unit cell volume *V*, inter-uranium distance d_{U-U}, relative expansion of unit cell volume $\Delta V/V$, Curie temperature T_C, Néel temperature T_N.

Some geometrical criteria have to be fulfilled to make the hydride formation possible. Geometrical requirements include sufficient size for the interstitial positions and their arrangement in space.

1. Westlake's criterion states that available interstitial sites must have a spherical volume with the radius ≥ 40 pm [5-9].
2. The minimum H-H distance should be 210 pm.
3. According to the "Shoemaker's exclusion rule" two tetrahedra sharing the same face cannot be occupied simultaneously [10-12].

However one should keep in mind that there are always some exceptions from these rules due to the fact that the stability of the hydride is determined by many factors and none of them predominates in all cases.

2.3.2. Effect of "hydrogenation" on electronic structure and magnetism

One of the features of the electronic structures of metal hydrides is the formation of hydrogen-induced states below E_F of a metal that can be filled with added electrons. Hybridization of the valence states with the *s*-states of hydrogen lowers in energy of the electronic states in a host metal. The states formed in this way are of bonding character. The same number of antibonding states brought by hydrogen is expelled to higher energies above the Fermi level.

The finding of the formation of UH_3 shows how dramatic changes upon hydrogenation can occur in the actinide compounds. Metallic uranium crystallizes in orthorhombic structure (space group *Cmcm*) and does not show magnetic ordering. It is a weak Pauli paramagnet with the value of magnetic susceptibility $\chi = 4.9\times10^{-9}$ m^3/mol at room temperature. Two modifications of UH_3 hydride were reported. Both α-UH_3 (low temperature modification) [13] and β-UH_3 (high temperature modification) [14,15] crystallize in cubic *Pm3n* space group. Crystal structure of α-UH_3 can be considered as simple *bcc* packing of uranium atoms each surrounded by an icosahedron of the atoms of hydrogen. Therefore uranium atoms are separated in space and the lattice is held mainly by metal-hydrogen bonds. α-UH_3 is a ferromagnet with ordering temperature between 174 and 178 K. However, the α-UH_3 phase is difficult to prepare and it frequently contains a mixture of α- and β-phases. Crystal structure of β-UH_3 consists of two uranium sublattices. One uranium sublattice forms a *bcc* structure of widely spaced presumably magnetic metal atoms similar to what was observed for α-phase, whereas the second sublattice builds infinite chains of closely spaced uranium atoms, two in each cube phase. Band calculations showed that there should be major *f-f* overlap of the 5*f* functions for this distance, whereas the *bcc* sublattice seems to be the most likely candidate for local magnetic moments. β-UH_3 is also a ferromagnet with T_C in the range between 170 and 181 K. The measured paramagnetic moment $\mu_{eff} = 2.44$-$2.97\ \mu_B$ is below the expected value for the localized $5f^3$ (U^{+3} – 3.62 μ_B) or $5f^2$ (U^{+4} – 3.58 μ_B) state. It was shown by calculations that both α-UH_3 and β-UH_3 structures favor *f*-electron bonding with the hydrogen states, β-UH_3 more so than α-UH_3. The electronic specific heat coefficient of β-UH_3 ($\gamma = 28.5$ mJ/mol K^2) is nearly by a factor of three larger than that of metallic uranium.

2.4. UTX compounds

2.4.1. ZrNiAl structure

UTX compounds crystallize in one of four crystallographic structures (hexagonal ZrNiAl, GaGeLi, orthorhombic TiNiSi or cubic MgAgAs). ZrNiAl (space group $P\bar{6}2m$, atomic positions: U – 3*g* (x_U; 0; 0.5); T_1 – 1*b* (0; 0; 0.5); T_2 – 2*c* (1/3; 2/3; 0); X – 3*f* (x_X; 0; 0)) structure is a hexagonal structure with two types of basal planes separated by c/z, one with U and T atoms, and the other with T and X atoms.

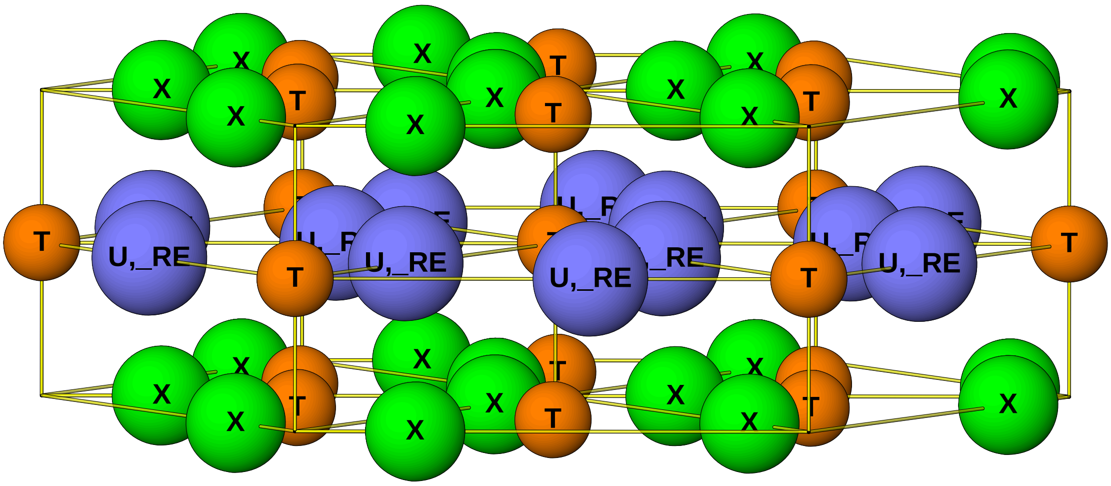

Fig. 3: Schematic representation of ZrNiAl structure type

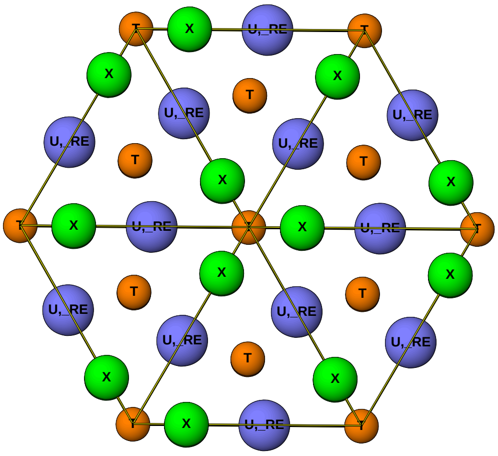

Fig. 4: Ground plan of ZrNiAl structure

Each uranium atom has four nearest uranium neighbours within the U–T layer and U–T layers are separated by the lattice parameter c. Inter-uranium distances in a direction are in the range of the Hill limit, in the c direction are somewhat larger.

There is strong hybridization along the nearest U direction. Magnetic moments are almost universally perpendicular to that direction (along the c-axis). The compounds crystallizing with ZrNiAl structure type are characterized by very high magnetic easy-axis anisotropy. The close packing within the basal plane leads to non-negligible $5f$-$5f$ overlap and to strong $5f$-d hybridization. As a consequence, a strong ferromagnetic coupling of the involved U magnetic moments appears. In order to estimate the type of interactions along the c-axis both, the $5f$-d (U-T) and $5f$-p (U-X) hybridization should be taken into account. In case the $5f$-d hybridization prevails a ferromagnetic coupling would rather occur and if the $5f$-p hybridization – antiferromagnetic.

2.4.2. $U_{1-x}Th_xCoSn$

UCoSn crystallizes in the ZrNiAl structure type with lattice parameters a = 714.6 pm, c = 399.4 pm [4]. It is a ferromagnet below T_C = 82 K [4]. The strong magnetic anisotropy with magnetic moments oriented along the c-axis was found. ThCoSn crystallizes in the same structure type and has been found to be a Pauli paramagnet down to 4.2 K [16]. The studies of the $U_{1-x}Th_xCoSn$ series, which follow in detail the disappearance of U magnetism when the U sublattice is diluted by a non-magnetic Th, were reported in Ref. 16.

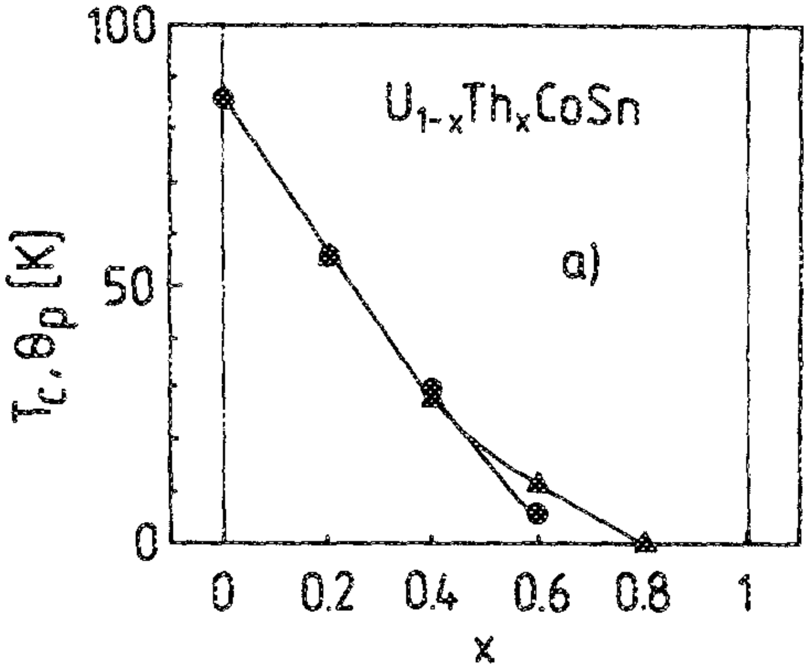

Fig. 5: Concentration dependence of T_C and θ_p [16].

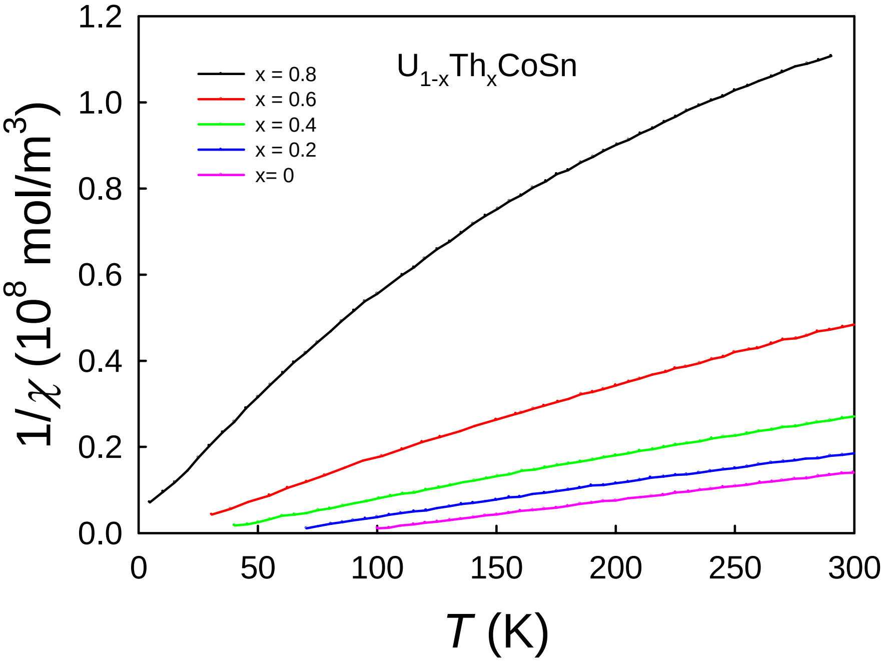

Fig. 6: Inverse susceptibility per mol f.u. as a function of temperature for $U_{1-x}Th_xCoSn$ [16]

2.5. U – metal

2.5.1. Structure and properties

Uranium metal has three crystalline phases.

The α-phase exists up to 668 ºC. This phase is orthorhombic (space group No. 63, Cmcm) with unit cell parameters *a* = 2.854 Å, *b* = 5.87 Å, *c* = 4.955 Å.

The β-phase exists between 668 and 775 ºC. This phase belongs to the space group $P4_2/mnm$, $P4_2nm$ or P4n2. Its unit cell parameters are *a* = 5.656 Å and *b* = *c* = 10.759 Å.

The γ-phase (between 775 ºC and 1134.8 ºC – the melting point) has a body-centered cubic structure with the cell parameter *a* = 3.524 Å.

α-Uranium exhibits three low-temperature charge density wave (CDW) phase changes at approximately $T(\alpha_3)$ = 23 K, $T(\alpha_2)$ = 36 K, $T(\alpha_1)$ = 42 K. In addition, it becomes superconducting below 2 K. α_1 is a structural and electronic transition, α_2 is an electronic transition. Below 23 K all 3 components of the CDW structure are commensurate with the underlying lattice. For temperatures bigger than 23 K but smaller than 43 K the CDW structure becomes incommensurate with the underlying structure [17].

Measurements of α-U, such as specific heat, show clear peaks for single crystals, but no peaks for polycrystals (the polycrystalline samples effectively wash out the signal over enough temperature range to loose the small peaks).

U-metal is a weak paramagnet and exhibits almost temperature-independent paramagnetism (room temperature value: $\approx 4\cdot10^{-9}$ m^3/mol).

2.5.2. Previous measurements performed by J. C. Lashley

This chapter is a review of measurements of uranium properties performed by J. C. Lashley at al. and published in 2001 [17]. These measurements were performed on the uranium crystals (in many respects the best so far studied U metal) grown by electrotransport through a molten salt bath of LiCl-KCl eutectic containing on the order of 3 wt. % UCl_3. The uranium was deposited onto a stainless steel cathode as dendrites in the form of parallelogram-edged platelets, often diamond shaped. These individual platelets within the dendrites are single crystals of α-uranium. Because the uranium was deposited at temperatures below the α-β transformation temperature, they were strain free and nearly perfect.

The electrical resistivity was measured using standard four-probe AC technique. The features associated with all three CDW (charge density waves) are clearly visible on the resistivity data (Fig. 7). The residual resistivity ratio (RRR) is about 115.

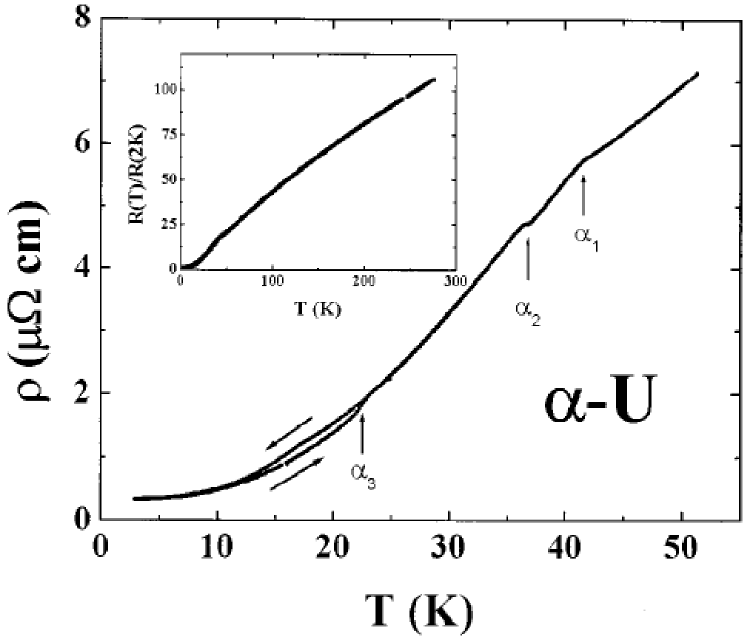

Fig. 7: The temperature dependence of the resistivity of uranium single crystal. Diagonal arrows denote the direction in which the temperature was changing during data acquisition. Vertical arrows denote the position of CDW features.

The specific heat is was measured in zero-magnetic field using an apparatus designed around a ^{3}He insert capable of attaining temperatures as low as 0.4 K. A semiadiabatic pulse technique was used to measure the specific heat from the lowest temperature up to 10 K, the isothermal technique was used to measure the specific heat from 10 to 100 K.

The three CDW can be seen on the specific heat data. The α_1 transition appears as a round hump in the specific heat data, the α_2 transition appears as a sharp peak and there is another broad peak at approximately 23 K (α_3 transition).

Analysis of the specific-heat data give an electronic specific heat

$\gamma = 9.13\ \mathrm{mJ \cdot mol^{-1} \cdot K^{-2}}$.

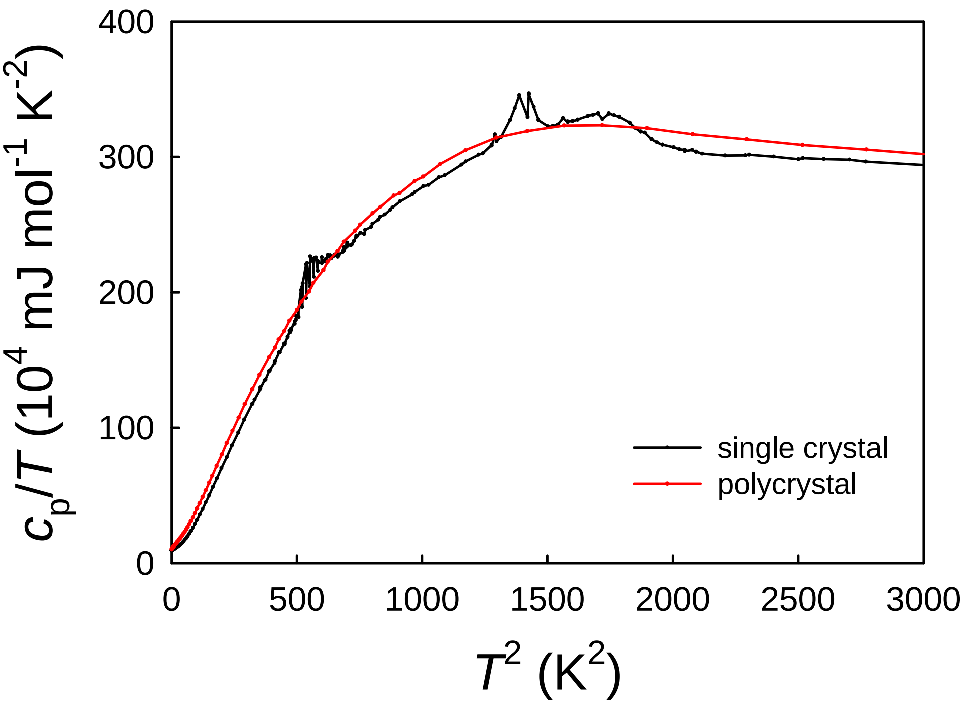

Fig. 8: Complete illustration of the effect of purity/crystal quality on the CDW transitions.

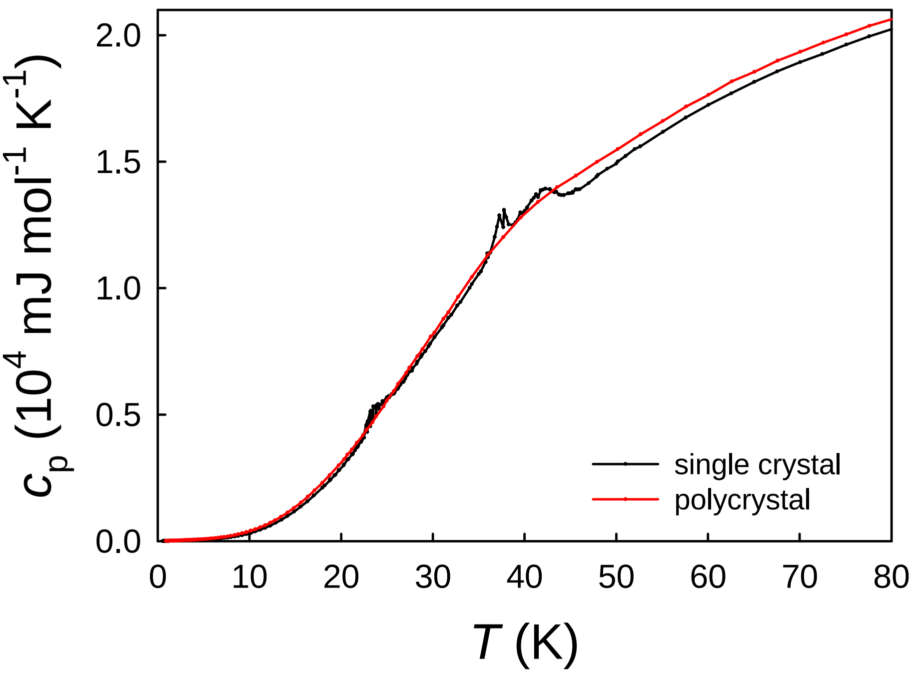

Fig. 9: Temperature dependence of specific heat of U-metal measured by Lashley [17] on single crystal and polycrystalline sample.

3. Experimental

3.1. Hydrides synthesis

As a standard, following procedure was applied. Bulk material obtained from arc melting was crushed into submillimeter particles and loaded in a reactor for hydrogenation. Fig.10 shows a scheme of the hydrogenation equipment. Before hydrogenation the surface of the sample pieces was activated by heating up to T = 523 K for 2 hours in dynamic vacuum ($p \approx 10^{-6}$ mbar) in order to desorb surface contaminants. Hydrogenation was performed by exposing an activated material to H_2 (p = 110 bar) and subsequent thermal treatment up to T = 773 K. Hydrogen absorption was registered by a pressure drop, however at such relatively high pressures it was impossible to determine the stoichiometry of the hydride with an acceptable accuracy (due to the thermal drift of the high-pressure gauge, etc.). To quantify the amount of absorbed hydrogen, samples of hydrides were decomposed in vacuum in closed volume by heating up to T = 923 K. By the amount of hydrogen released the stoichiometry of the hydrides was determined. The error bar of the hydrogen content determined by volumetric method depends on the amount of the sample decomposed and typically does not exceed ±0.1 H/f.u.

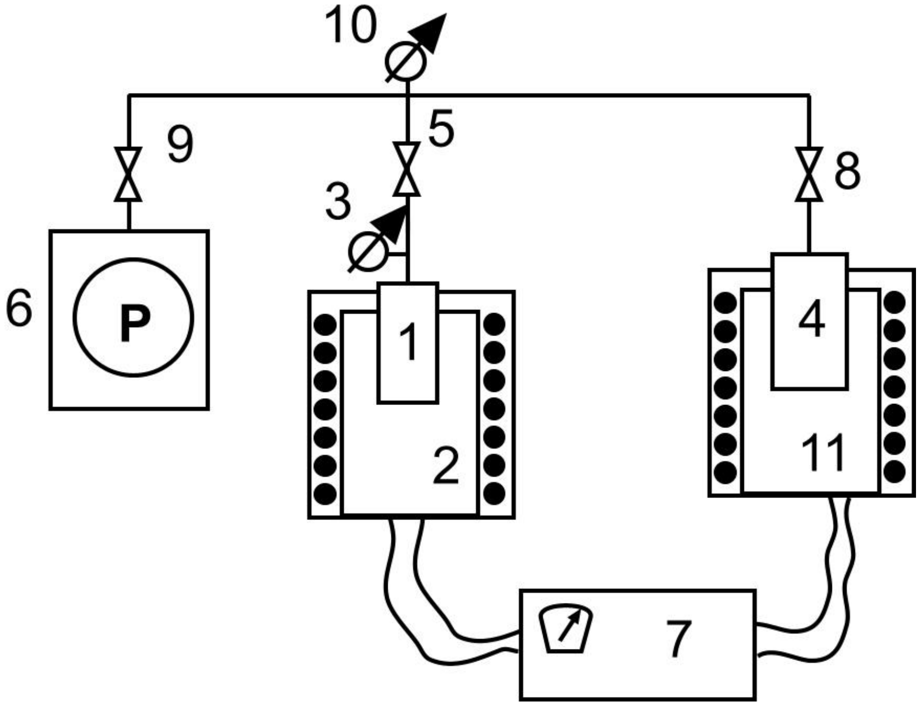

Fig. 10: The scheme of hydrogenation equipment: 1 – reactor; 2, 11 – furnaces; 3, 10 – vacuum gauges; 4 – $LaNi_5$ container with H_2 or D_2; 5, 8, 9 – valves; 6 – vacuum pumps (turbomolecular + membrane roughing pump); 7 – temperature control unit.

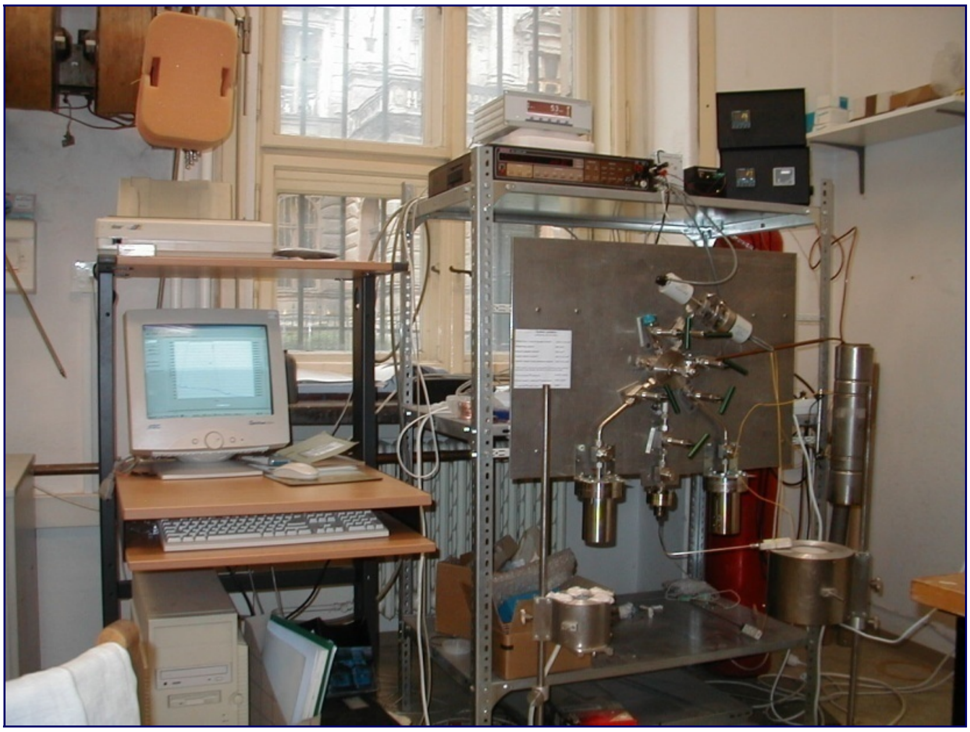

Fig. 11: Hydrogenation equipment at MFF UK.

3.2. Decomposition studies

3.2.1. Decomposition experiment

The stoichiometry of synthesized hydrides was determined by the decomposition in closed volume at $T \approx 923$ K. Samples of approximately 100 mg were loaded in reactor of the closed volume of 136.7 cm^3. Performed decomposition had three stages. At first the sample was linearly heated up to 650 °C with the heating rate 4 K/ min, then the temperature was left constant. After several minutes the heater was turned off. It is the stage three when the temperature is decreasing. During the first stage the pressure is increasing because the hydrogen is released from the compound. From the amount of hydrogen released, the stoichiometry of the hydride can be determined using an equation of state (see below). The cooling of the whole system, necessary to achieve uniform temperature used as input for the equations, can lead in some cases to a small re-absorption of H gas. Therefore we undertake is selected cases a second desorption cycle, after pumping out all released hydrogen. The amount of H released in the second cycle does not exceed for the materials as UCoSn more than 5% of the release in the 1st cycle, and its effect on the stoichiometry determination is small.

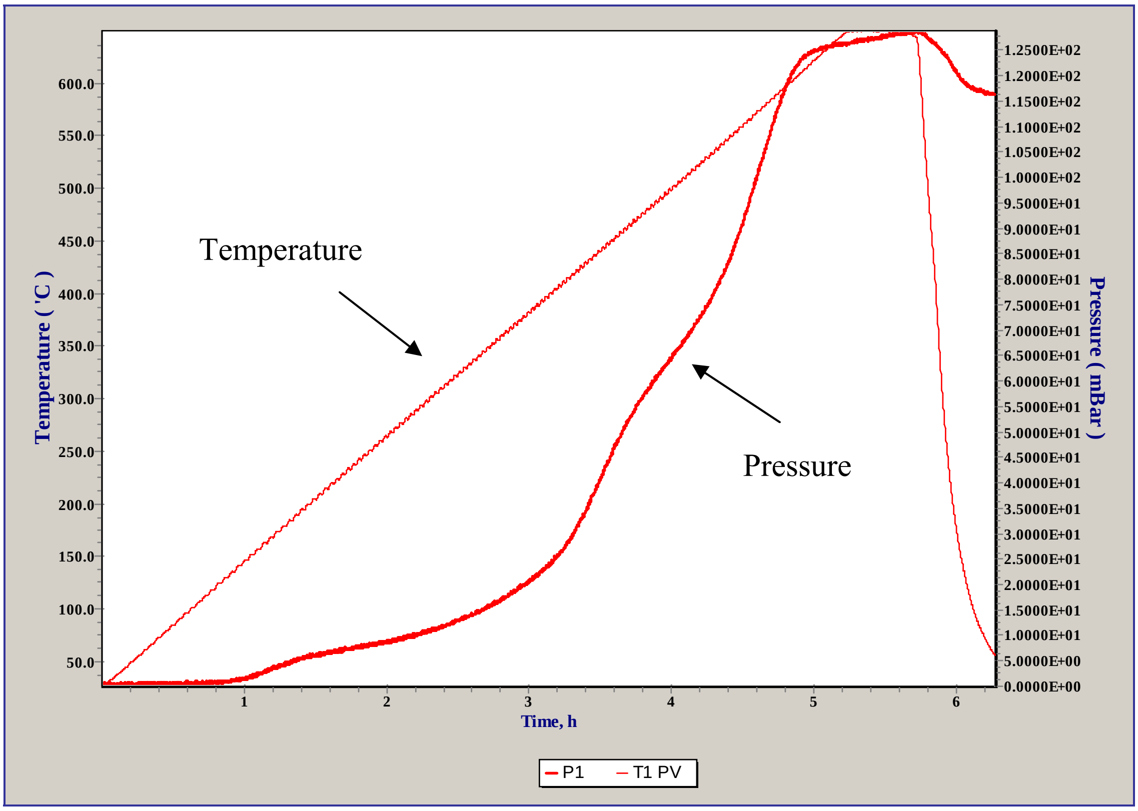

Fig. 12: Decomposition curve of hydride performed in closed volume 136.7 cm^3.

3.2.2 Hydrogen content determination

In general, three types of equations can describe the state of the real gas:

a. State equation of ideal gas (Mendeleev-Clapeyron)

$$pV = \frac{m}{M} RT \quad , \qquad (8)$$

where p is pressure in the closed volume V, filled with gas of the weight m and molar mass M, T is absolute temperature and R is the universal gas constant R = 8.31 J/mol·K.

The dependence of pressure in a certain volume on the gas quantity is a straight line, the slope of which changes with the temperature.

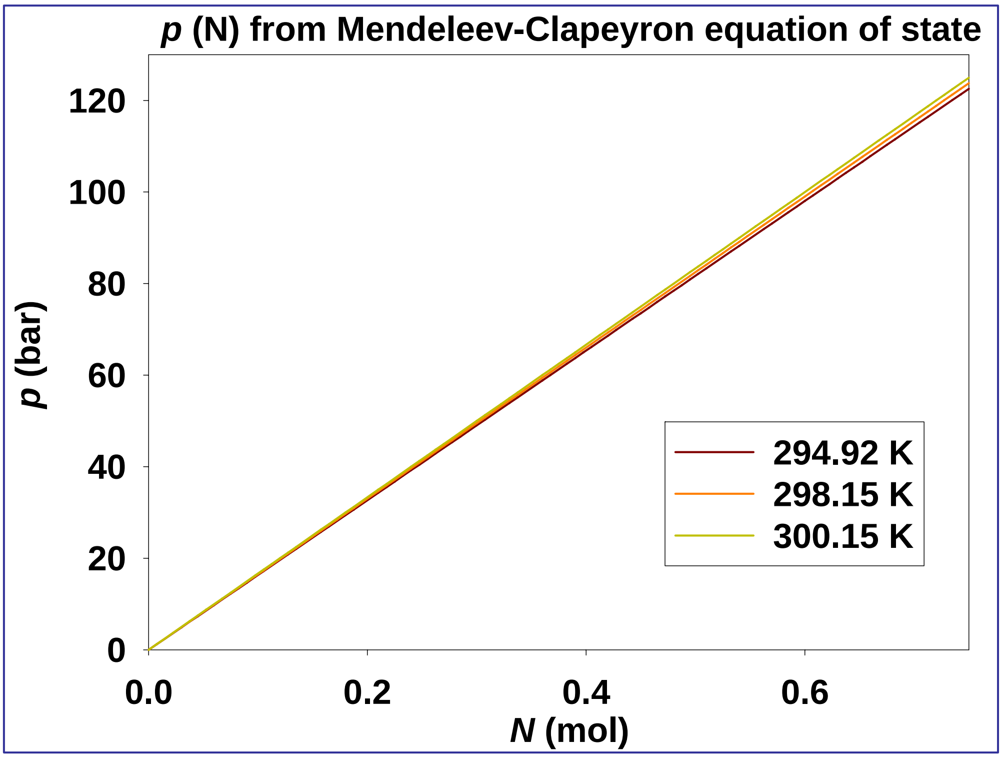

Fig. 13: Dependence of the pressure in V = 150 cm^3 at different temperatures calculated from the Mendeleev-Clapeyron equation of the state for the ideal gas.

b. Van der Waals equation

$$\left[p+\left(\frac{m}{M}\right)^2\cdot\frac{a}{V^2}\right]\cdot\left[V-\frac{m}{M}\cdot b\right]=\frac{m}{M}RT\,, \tag{9}$$

where p, V, m, M, T and R are the same quantities as in Mendeleev-Clapeyron equation of the state for the ideal gas and a and b are gas specific correction coefficients.

Parameters a and b are closely related to the critical parameters of the corresponding gas:

$$a=3p_{cr}\cdot V_{cr}^2; b=\frac{V_{cr}}{3}; R=\frac{8p_{cr}\cdot V_{cr}}{3T_{cr}} \tag{10}$$

In the vicinity of T_{cr} one should take into account the constant variation of R from as to gas. Far from T_{cr} the value of R is the same for all gasses. Since for hydrogen T_{cr} is about 30 K where R = 6.76 J/mol·K, there is no need to take this dependence into account. The critical parameters for same gasses are the following:

gas	T_{cr} (K)	p_{cr} (10^5 Pa)	V_{cr} (10^{-3} m^3/kg)
H_2	33.2	13.29	32.26
N_2	126.0	33.93	3.22
O_2	164.3	50.34	2.32
Cl_2	417.1	77.08	1.75
H_2O (vapour)	647.25	220.53	2.50

Table 2: Critical parameters of some gasses.

For H_2:

$a = 1.64 \cdot 10^{-2}$ or $2.476 \cdot 10^{-2}$ (more exactly) Pa·m^6/mol^2

and

$b = 2.2 \cdot 10^{-5}$ or $2.661 \cdot 10^{-5}$ (more exactly) m^3/mol.

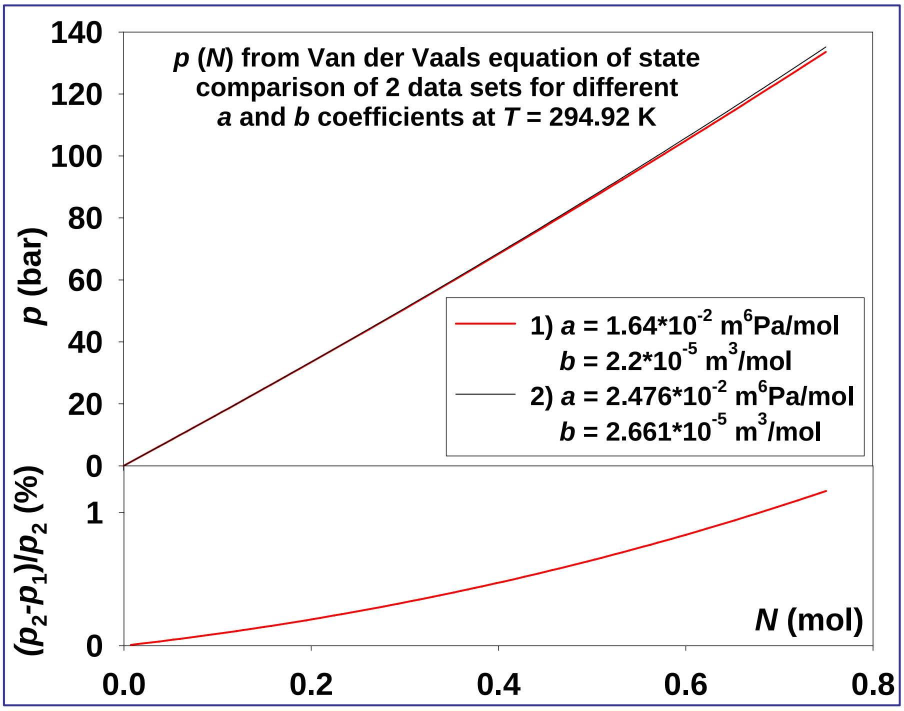

Fig. 14: Dependence of pressure in $V = 150$ cm^3 calculated from the Van der Waals equation of the state for the real gas. We have 2 sets of coefficients a and b, the second of which seems to be more precise. The difference between p (N) calculated for both (a, b) sets is shown on the lower panel.

In the case of Van der Waals equation of state (Fig. 14) the same dependence of pressure in $V = 150$ cm^3 on the gas unity, as plotted in Fig. 13, looks different: it has a slight curvature at high pressures, and gives higher absolute values of pressure at the same N than the Mendeleev-Clapeyron equation of the state for the ideal gas.

c. Advanced calculations (derived from Lennard-Jones potential)

The virial expansion derived from the Lennard-Jones potential with the precision up to the second term has the following form:

$$\frac{pV_m}{\mathrm{R}T} = 1 + \frac{B}{V_m} + \frac{C}{V_m^{\;2}}, \tag{11}$$

Where p, R and T have the same meaning as above, V_m is molar volume. B and C are virial coefficients.

$$B = \frac{2}{3}\pi \mathrm{N}_A \sigma^3 \int_0^\infty [e^{-u(x)/kT} - 1]x^2 dx$$

$$u(x) = 4\varepsilon[x^{-12} - x^{-6}]$$

$$x = r/\delta, \text{etc....}$$

The virial coefficients B, C are tabulated.

The tabulated values B^*, C^* vs. T^* are related in the following way to B, C vs. T from equation:

$$C = C^* b_o^2,\; T^* = kT/\varepsilon,\; B(T) = b_0 B^*(T^*),\; b_0 = \frac{2}{3}\pi N_A \sigma^3$$

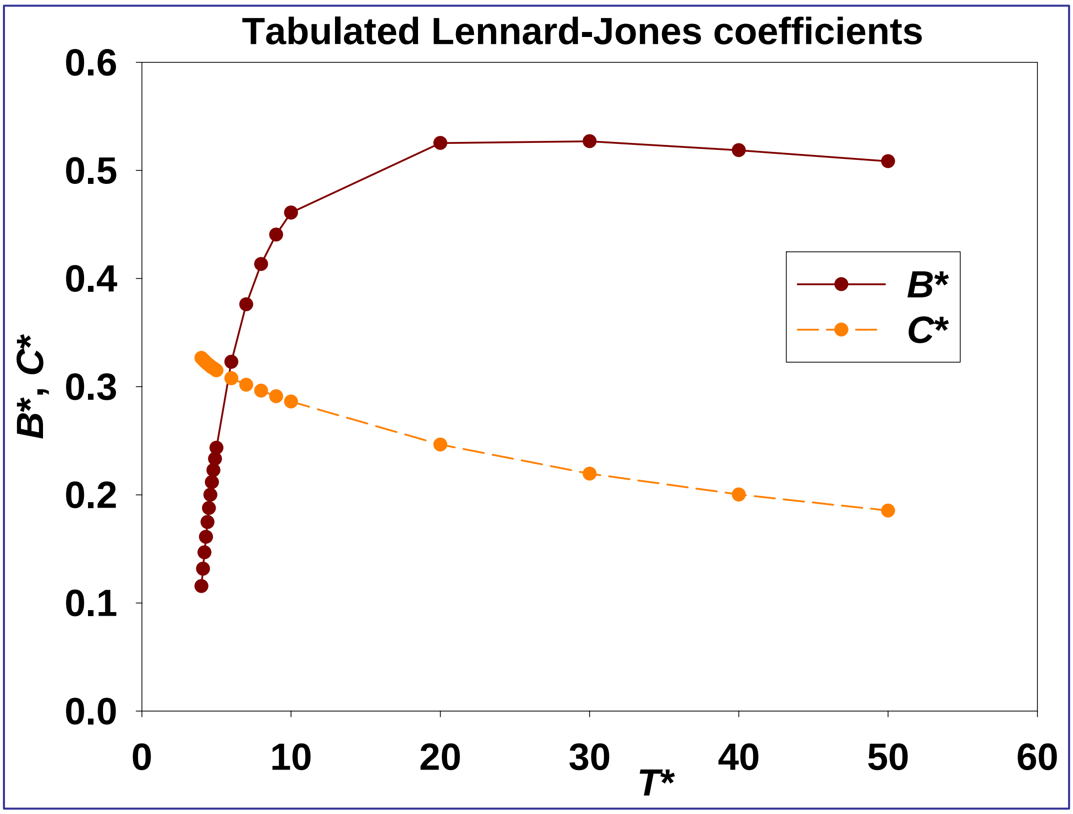

Fig. 15: Tabulated Lennard-Jones coefficients *B** and *C** vs. *T**.

d. Analysis

It appears that for hydrogen all three techniques described above provide almost similar precision in the pressure range of $p < 30$ bar at $T \approx 300$ K. When pressure exceeds 30 bar, substantial discrepancy, reaching 9 % at $p \approx 120$ bar, can be observed between the values calculated using different methods. Since Van der Waals and Leonard-Jones equations are taking into account the physical properties of the real gas like compressibility or final molecule size we are inclined to assume that the values obtained from them are more exact.

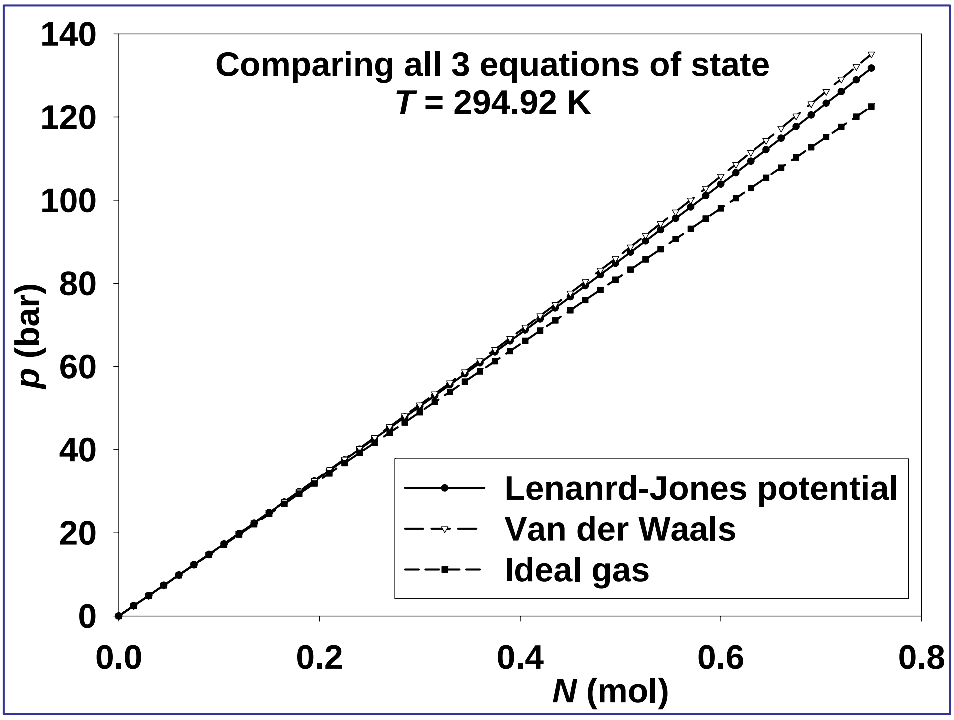

Fig. 16: The difference of absolute values *p* (N) calculated using different models.

3.3. X-ray diffraction studies

X-ray analysis was used for sample characterization and phase analysis: the diffraction patterns of intermetallic compounds were taken before and after hydrogenation. The data were collected on XRD-3003 (Seifert) diffractometer in a step regime (step 0.04º of 2θ). The diffraction can be considered as the reflection of X-ray beam from the atomic planes of the crystal and can be described by the Bragg law:

$$2d \sin\theta = n\lambda \tag{12}$$

where n – an integer, called the order of reflection

d – the interplanar distance

θ – an angle of reflection

λ – wavelength of radiation.

The main disadvantage of the X-ray diffraction is that light atoms, including hydrogen having just one electron, cannot be detected. Since X-rays interact with the electronic cloud of an atom, atoms with atomic number $Z < 13$ are almost "invisible" for X-rays and consequently the neutron diffraction experiment has to be performed to get the information where the hydrogen is placed.

The crystal structure refinement, based on the analysis of obtained X-ray powder patterns, has been performed by FullProf software [18], which is based on the Rietveld algorithm [19].

In the Rietveld refinement a mathematical model is assumed to represent the experimental pattern. In particular, when a structural model is available, then the intensity y_{io} observed at the ith step may be compared with the corresponding intensity y_{ic} calculated via the model. According to Rietveld, the model may be refined by minimizing by a least-squares process the residual

$$S = \sum w_i \left| y_{io} - y_{ic} \right|^2 \tag{13}$$

where w_{i}, given by

$$\left(w_i\right)^{-1} = \sigma_i^2 = \sigma_{ip}^2 + \sigma_{ib}^2, \tag{14}$$

is a suitable weight. σ_{ip} is the standard deviation associated with the peak (usually based on the counting statistics) and σ_{ib} is that associated with the background intensity y_{ib}.

y_{ic} is the sum of the contributions from the neighboring Bragg reflections and from the background:

$$y_{ic} = s\sum_{k} m_k L_k |F_k|^2 G(\Delta\theta_{ik}) + y_{ib}, \tag{15}$$

where s is a scale factor, L_{k} is the Lorentz-polarization factor for the reflection k, F_{k} is the structure factor, m_{k} is the multiplicity factor, $\Delta\theta_{\mathrm{ik}} = 2\theta_i - 2\theta_k$, where $2\theta_k$ is the calculated position of the Bragg peak corrected for the zero-point shift of the detector, and $G(\Delta\theta_{\mathrm{ik}})$ is the reflection profile function.

The parameters to adjust by refinement include unit cell, atomic positional and thermal parameters, and parameters defining the functions G and y_{ib}.

The quality of the agreement between observed and calculated patterns is measured by a set of the following nowadays conventional factors, based on Eqn. (13):

1. the profile $R_p = \sum|y_{io} - y_{ic}| / \left(\sum y_{io}\right)$
2. the weighted profile $R_{wp} = \left[\sum w_i (y_{io} - y_{ic})^2 / \sum w_i y_{io}^2\right]^{1/2}$
3. the Bragg $R_B = \sum|I_{ko} - I_{kc}| / \left(\sum I_{ko}\right)$. The values I_{ko} are obtained by partitioning the raw data in accordance with the I_{kc} values of the component peaks.
4. the expected $R_E = \left[(N-P)/\left(\sum w_i y_{io}^2\right)\right]^{1/2}$, where N and P are the number of profile points and refined parameters respectively.
5. the goodness of fit $GofF = \sum w_i (y_{io} - y_{ic})^2 / (N-P) = (R_{wp}/R_E)^2$, which should approach the ideal value of unity.

The most meaningful indices for the progress of refinement are R_{wp} and $GofF$ since they contain the quantity being minimized in the numerator. Also R_B is of considerable use since it depends on the fit of structural parameters more than on the profile parameters.

3.4. Magnetic studies

Measurements of AC and DC magnetization were performed by means of a Quantum Design PPMS extraction magnetometer at the Joint Laboratory for Magnetic Studies. Quantum Design PPMS extraction magnetometer was used for the measurements of AC and DC susceptibility and magnetization curves of the synthesized hydrides. For comparison, the parent compounds were studied in the same experimental conditions. At the DC extraction method, the sample is moved through the detection coils and induces a voltage in the detection coil set according Faraday’s law. During AC measurement, an alternating field is applied to the measurement region and the sample is positioned in the center of the detection coil. The detection coils indicate how the applied field is changed by the presence of the sample. This method does not directly measure a sample’s magnetic moment, but it is very useful for examining the nature of magnetic phase transitions. AC susceptibility typically diverges at the critical temperature of a ferromagnetic phase transition. For these measurements the samples were crushed into powder and fixed by acetone-soluble glue to prevent the orientation in external fields. We have performed our measurements in the temperature range from 2 to 300 K, in external magnetic fields up to 9 T.

3.5. Resistivity measurements

This experiment was performed only on uranium metal sample.

The DC resistivity was measured on the PPMS measuring system using a four-wire technique. Using four wires to attach the sample to a sample puck eliminates the contribution of the leads and joints to the resistance measurement. In four-wire resistance measurement current is passed through the sample via two current leads and two separate voltage leads measure the potential difference across the sample. So we can calculate the resistance with Ohm’s law.

$$R = U/I \qquad (16)$$

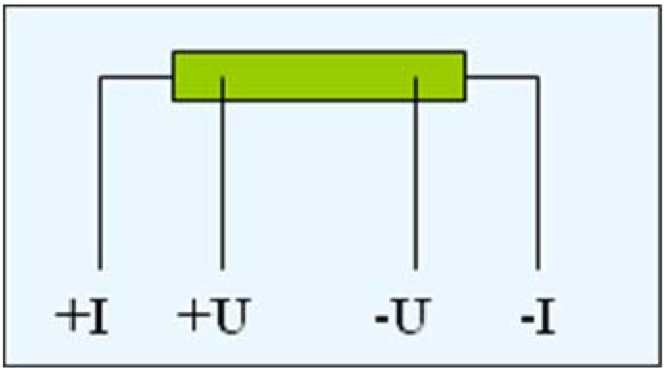

Fig. 17: Scheme of four-wire technique for resistivity measurement.

3.6. Heat capacity measurements

This experiment was performed only on Uranium metal sample.

The heat capacity measurements were performed using the PPMS measuring system in the temperature range 1.8-300 K. After the installation of the sample, high vacuum was reached within the chamber and sample was cooled down to the required temperature T. For measuring the specific heat of a material, a heat pulse $Q(t)$ is supplied to the sample within the time interval (t_1-t_2), producing a change in temperature ΔT. The temperature of the sample then returns to its initial value with a relaxation time $\tau = C/\kappa$, where C is the specific heat of the sample and κ is the thermal conductance linking the sample to its surrounding.

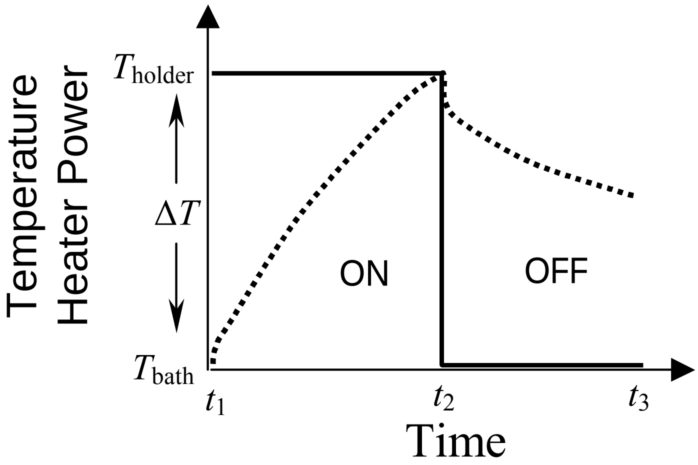

Fig. 18: Plot of temperature response in relaxation measurement

We can write heat-flow equation for one-dimensional case (the power loss through radiation is neglected):

$$C_{total}(T)\frac{dT}{dt} = Q(t) - \kappa_{wires}(T(t) - T_{bath}) \tag{17}$$

For the cooling curve we obtain:

$$T(t) = T_{bath} + (T_{holder} - T_{bath})\exp(-{}^{t}\!/_{\tau}) \tag{18}$$

T_{bath} is original temperature before heating process or is the temperature of the thermal bath. If poor thermal attachment of the sample to the platform produces a temperature difference between the two, the two-tau model is applied to measure the specific heat of the sample. This model simulates the effect of heat flowing between the sample holder and sample, and the effect of heat flowing between the sample holder and puck (bath). The following equation evaluate two-tau model:

$$\begin{aligned} C_{holder}\frac{dT_{holder}}{dt} &= Q(t) - \kappa_{wires}(T_{holder}(t) - T_{bath}) + \kappa_g(T_{sample}(t) - T_{holder}(t)) \\ C_{sample}\frac{dT_{sample}}{dt} &= -\kappa_g(T_{sample}(t) - T_{holder}(t)) \end{aligned} \tag{19}$$

κ_g is the thermal conductance between the sample and sample holder due to the grease. C_{holder} is the heat capacity of the sample holder and $C_{total} = C_{sample} + C_{holder}$.

Solution of the set of Eqns (c) for cooling curve is:

$$T(t) = T_{bath} + (T_{holder}(t) - T_{bath})\exp(-{}^{t}\!/_{\tau_1}) - (T_{holder}(t) - T_{sample})\exp(-{}^{t}\!/_{\tau_2}) \tag{20}$$

The temperature of the sample changes exponentially with relaxation times τ_1, τ_2. For calculating specific heat, least-square fitting algorithm is applied. The sensitivity of the fit deviation to small variations in the fitting parameters is used to estimate the standard errors for the specific heat.

4. Results and discussion

Hydrogen absorption properties of $U_{1-x}Th_xCoSn$ were studied on 5 compounds with $x = 0.2$, 0.4, 0.6, 0.8, and 1.

Before performing hydrogenation the samples were crushed into submillimeter powder. The surface was subsequently activated by heating up to T = 523 K for 2 hours in dynamic vacuum ($p \approx 10^{-6}$ mbar) in order to desorb surface contaminants. The synthesis was performed at hydrogen pressure 120 bar and at temperature $T = 773$ K. The stoichiometry was determined by the decomposition in closed volume at $T \approx 923$ K. The amount of absorbed hydrogen decreases from 1.4 to 0.8 H/f.u. with increasing Th concentration (Fig. 23).

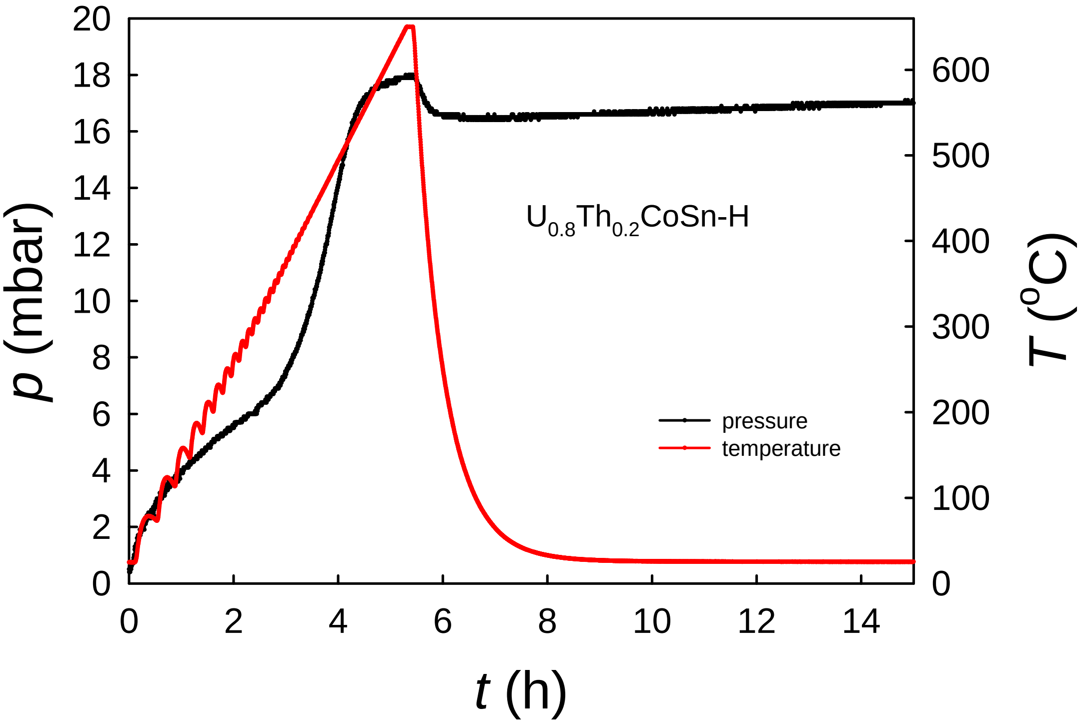

Fig. 19: Decomposition curve of $U_{0.8}Th_{0.2}CoSn$ hydride in closed volume of 136.7 cm^3. Red curve represents temperature, black one represents temperature dependence of pressure in closed system.

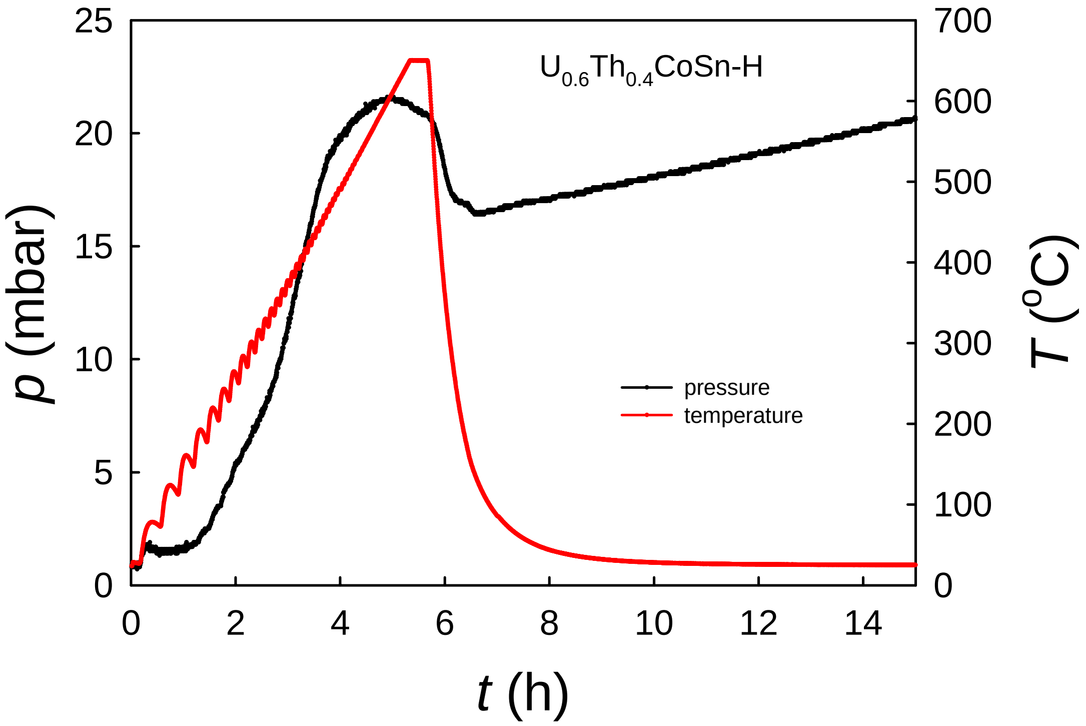

Fig. 20: Decomposition curve of $U_{0.6}Th_{0.4}CoSn$ hydride in closed volume of 136.7 cm^3. Red curve represents temperature, black one represents temperature dependence of pressure in closed system.

.

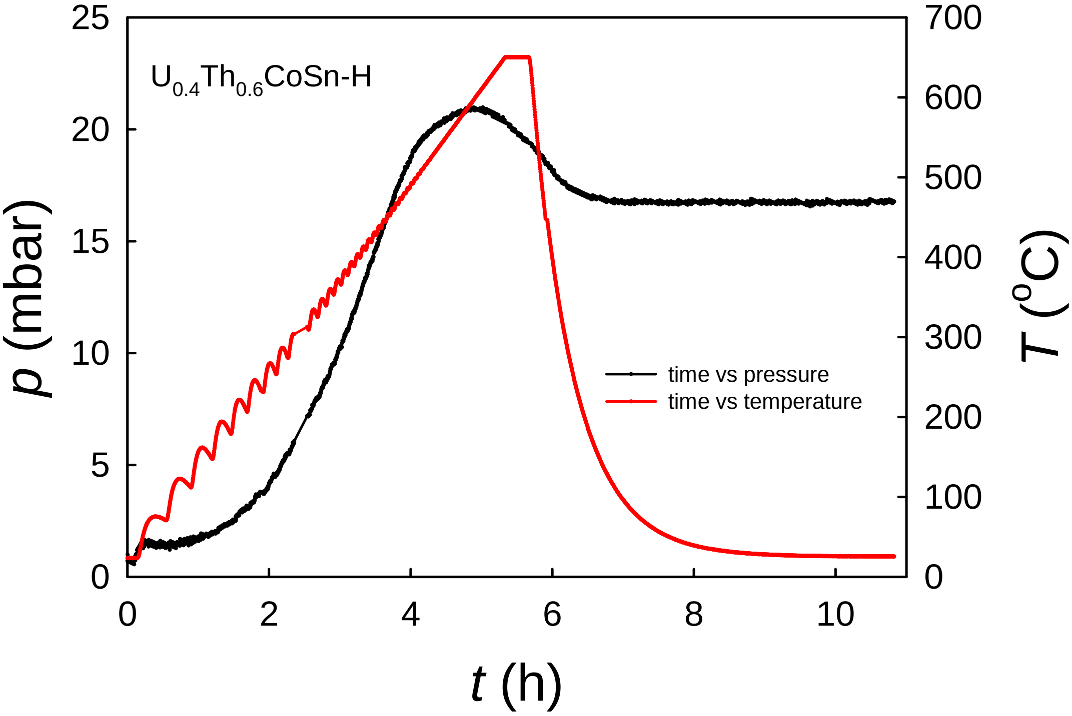

Fig. 21: Decomposition curve of $U_{0.4}Th_{0.6}CoSn$ hydride in closed volume of 136.7 cm^3. Red curve represents temperature, black one represents temperature dependence of pressure in closed system.

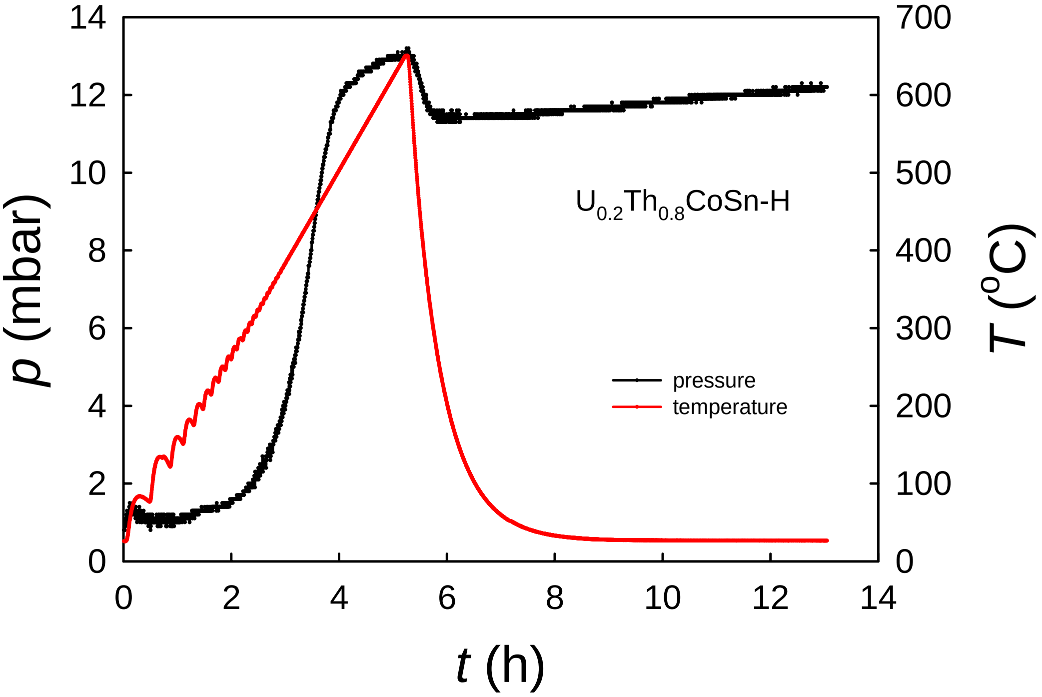

Fig. 22: Decomposition curve of $U_{0.2}Th_{0.8}CoSn$ hydride in closed volume of 136.7 cm^3. Red curve represents temperature, black one represents temperature dependence of pressure in closed system.

.

As seen from Fig.19 (Red curve represents temperature, black one represents pressure), the decomposition has three stages. At first the sample was linearly heated up to 650 °C then the temperature was left shortly constant. After several minutes the heater was turned off. It is the stage three in the Fig.20 where the temperature is decreasing. The stage 1 in this case reveals a peculiarity. Heating the sample (as well as a part of the system) should lead to a pressure increase. But in the presented cases (Fig. 20, 21) it reaches a maximum for ≈ 580 °C and then starts to decrease. This can be attributed to a partial decomposition and the formation of a more stable hydride UH_3. Because of this effect it is more complicated to determine the stoichiometry of decomposed hydride. Our determined stoichiometry can be taken as lower estimate. In other case the drop of pressure occurs after the temperature is decreasing.

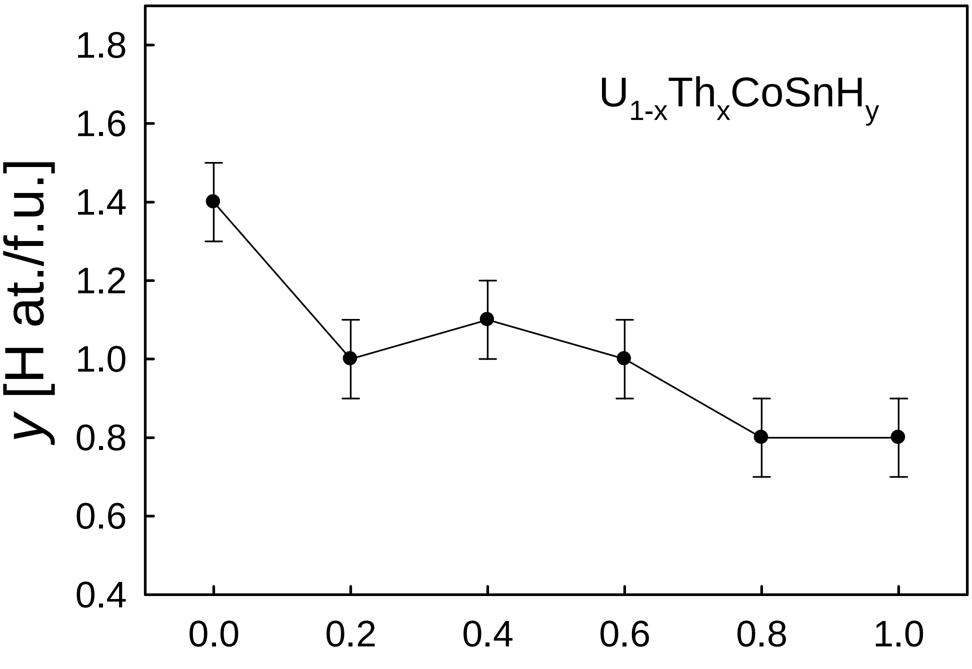

Fig. 23: Dependence of H concentration as determined by the desorption experiment in the $U_{1-x}Th_xCoSnH_y$ system as a function of Th concentration x. The line is a guide for eye.

Crystal structure of the initial compounds and of the synthesized hydrides was studied by X-ray powder diffraction. X-ray powder diffraction studies showed that ZrNiAl structure type is preserved both for the initial compounds and for the hydrides throughout the whole series. Hydrogenation leads to a unit cell expansion in all cases (ranging between 3.0% and 3.6%) what can be seen from shift of diffraction peaks (Fig. 24 and 25). Both lattice parameters increase in the hydride, but the increment of *c* is increasing with increasing Th concentration while increment of *a* is reduced (Fig. 26). The results of the crystal structure refinement of (U,Th)CoSn compounds and their hydrides are summarized in Table 3.

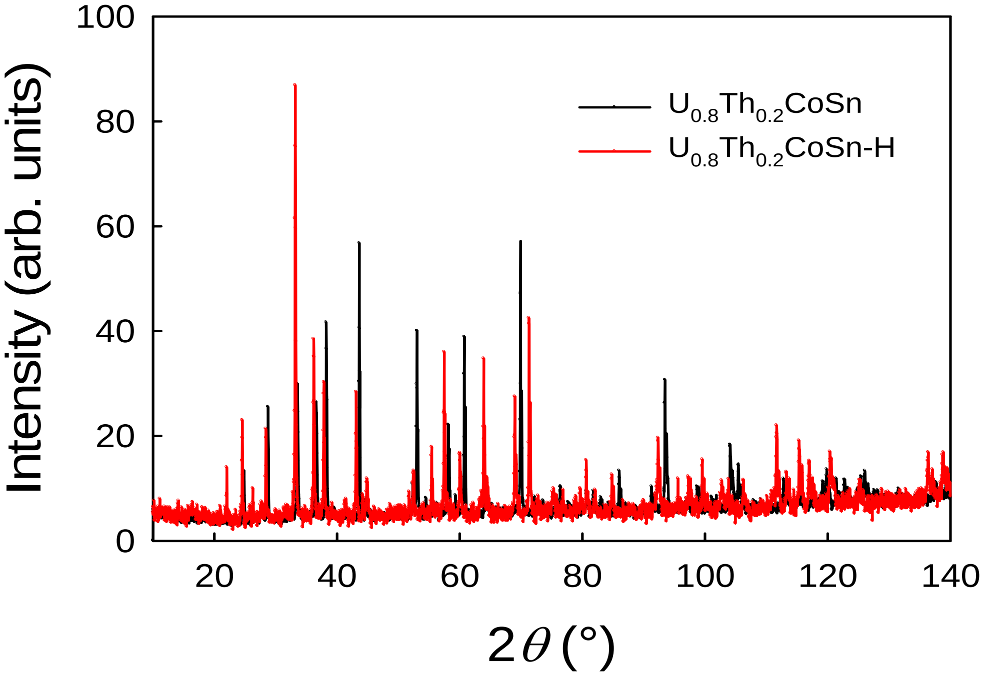

Fig. 24: Comparison of X-ray patterns of $U_{0.8}Th_{0.2}CoSn$ and its hydride.

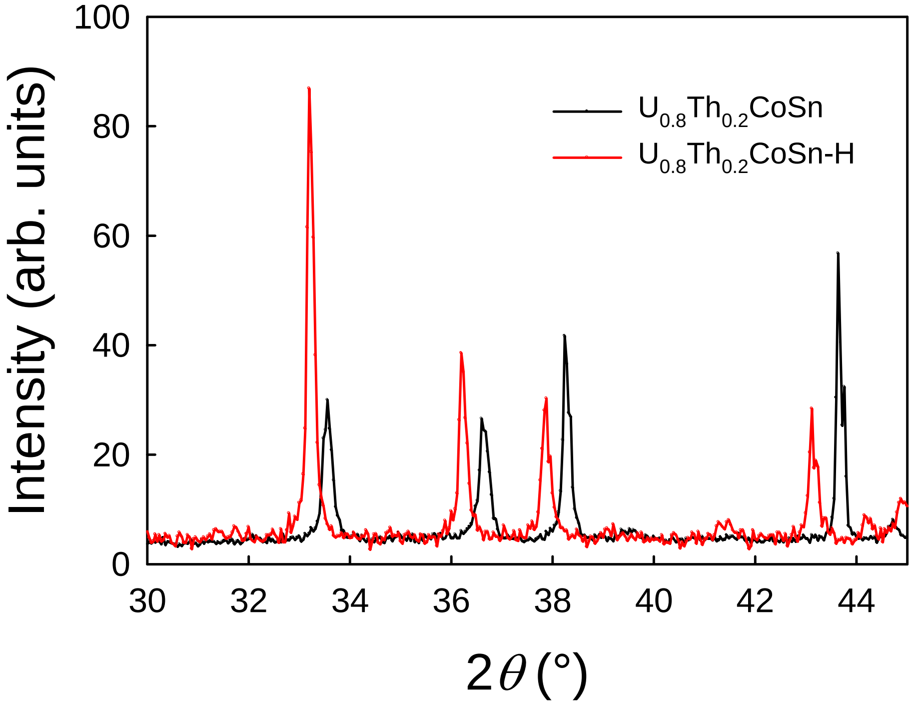

Fig. 25: Comparison of X-ray patterns of $U_{0.8}Th_{0.2}CoSn$ and its hydride (detail).

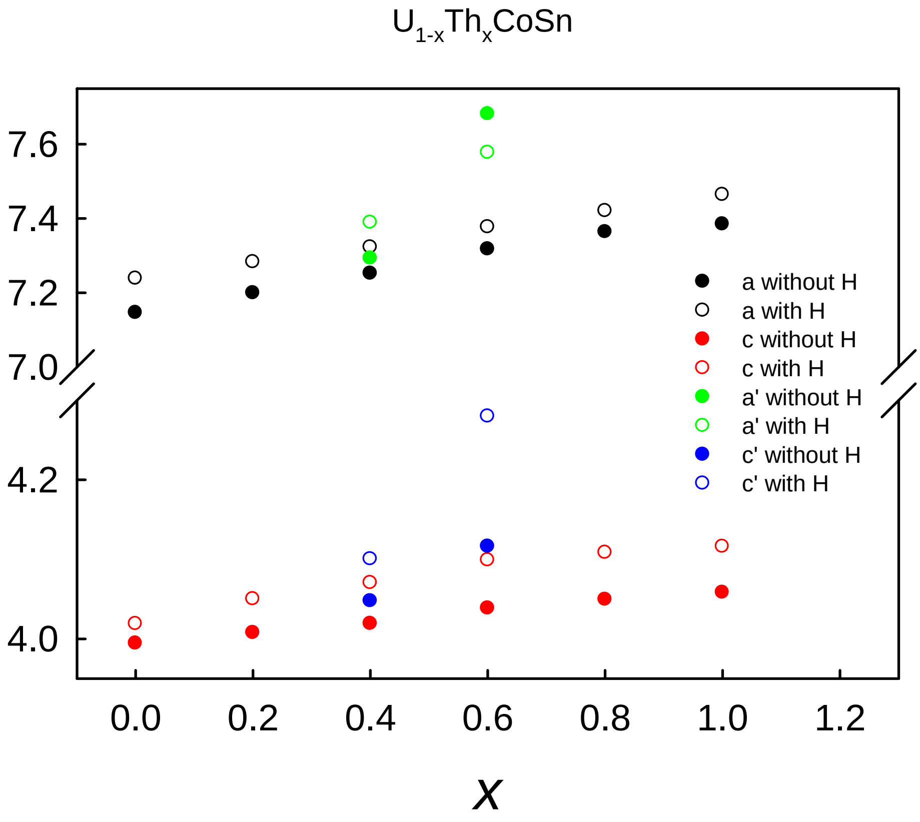

Fig. 26: Concentration dependence of lattice parameters of $U_{1-x}Th_xCoSn$ and their hydrides. Dashes denote the second phase.

	a (Å)	*c* (Å)	Δ*a*/*a* (%)	Δ*c*/*c* (%)	Δ*V*/*V* (%)
UCoSn	7.1459	3.9943	-	-	-
UCoSn-H	7.2386	4.0189	1.297	0.616	3.243
$U_{0.8}Th_{0.2}CoSn$	7.1992	4.0076	-	-	-
$U_{0.8}Th_{0.2}CoSn$-H	7.2830	4.0501	1.164	1.060	3.425
$U_{0.6}Th_{0.4}CoSn$	7.2503 7.2925	4.0192 4.0474	-	-	-
$U_{0.6}Th_{0.4}CoSn$-H	7.3235 7.3894	4.0710 4.1002	0.978 1.329	1.279 1.305	3.269 4.024
$U_{0.4}Th_{0.6}CoSn$	7.3189 7.6813	4.0396 4.1162	-	-	-
$U_{0.4}Th_{0.6}CoSn$-H	7.3733 7.5777	4.0992 4.2797	0.814 -1.347	1.501 3.972	3.16042 1.189
$U_{0.2}Th_{0.8}CoSn$	7.3634	4.0493	-	-	-
$U_{0.2}Th_{0.8}CoSn$-H	7.4201	4.1095	0.776	1.459	3.040
ThCoSn	7.3848	4.0582	-	-	-
ThCoSn-H	7.4638	4.1159	1.070	1.424	3.605

Table 3: Comparison of crystal structure parameters of (U,Th)CoSn compounds and their hydrides obtained in this work. Lattice parameters *a* and *c*, unit cell volume *V*, relative increase of lattice parameters (*a*, *c*) and volume change with respect to the parent compounds

The studies of magnetic properties of (U,Th)CoSn and their hydrides were performed at PPMS measurement system in the temperature range 2-300 K and applying magnetic fields up to 9 T. UCoSn is a ferromagnet below T_C = 82 K [16]. ThCoSn has been found to be a Pauli paramagnet down to 4.2 K [18].

Hydrogenation does not change the type of magnetic ordering for all compounds, but modifies ordering temperature (Fig. 30). Values of Curie temperatures were determined from AC-susceptibility curves shown on Fig. 27 and 28 (The curves have been rescaled for better comparison.).

AC susceptibility measurement was used because there can be seen sharp peaks on real part of magnetization at the transition temperatures. AC susceptibility typically diverges at the critical temperature of a ferromagnetic phase transition.

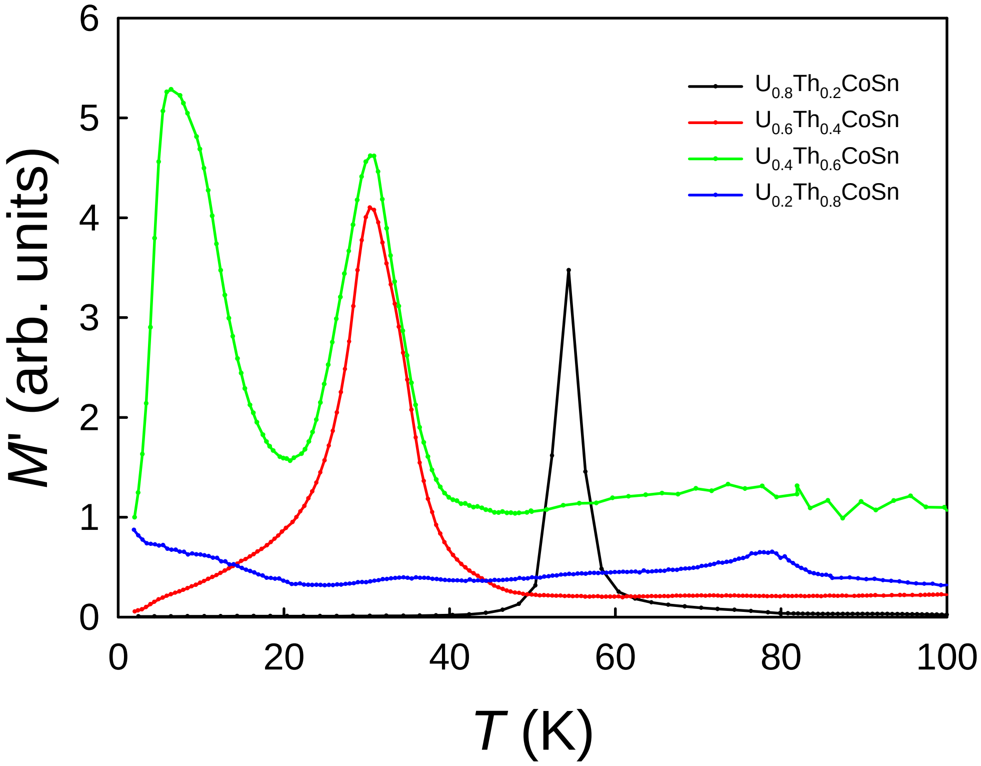

Fig. 27: Rescaled AC susceptibilities of $U_{1-x}Th_xCoSn$.

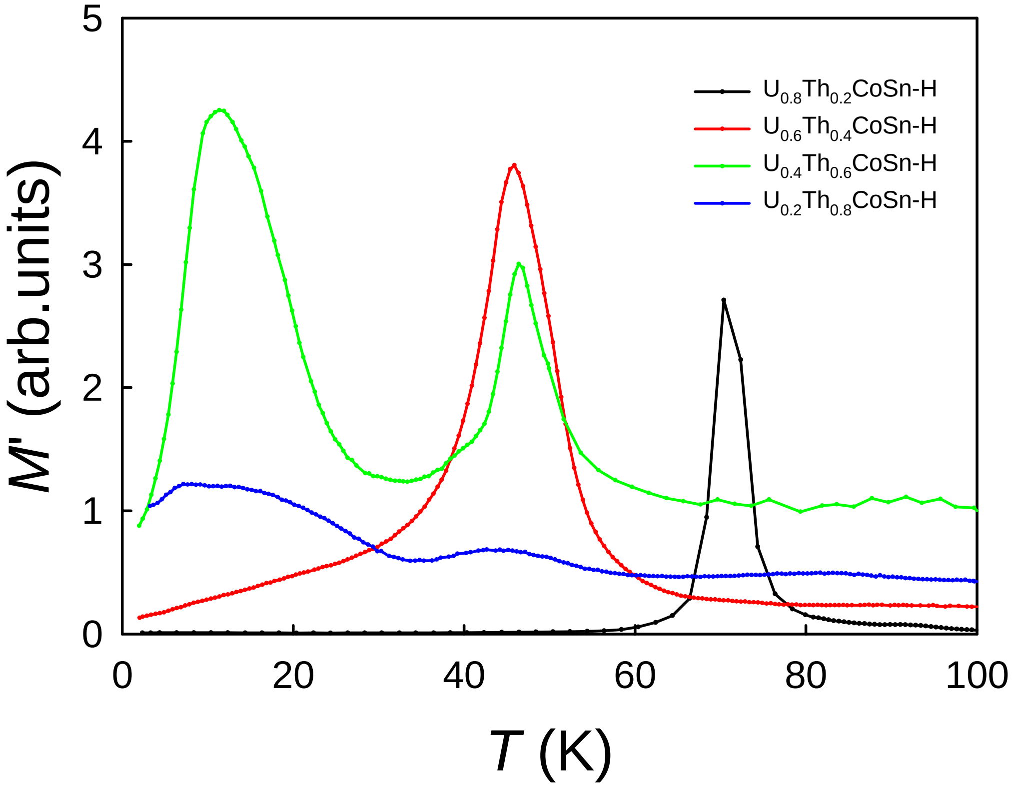

Fig. 28: Rescaled AC susceptibilities of $U_{1-x}Th_xCoSn$-H.

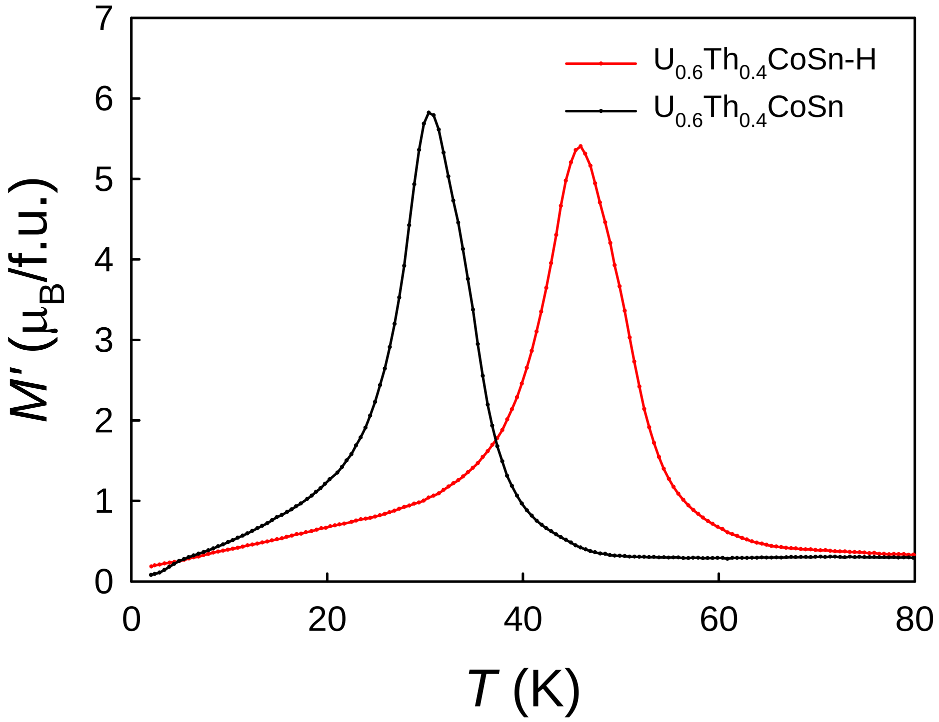

Fig. 29: AC-susceptibility of $U_{0.6}Th_{0.4}CoSn$ and its hydride.

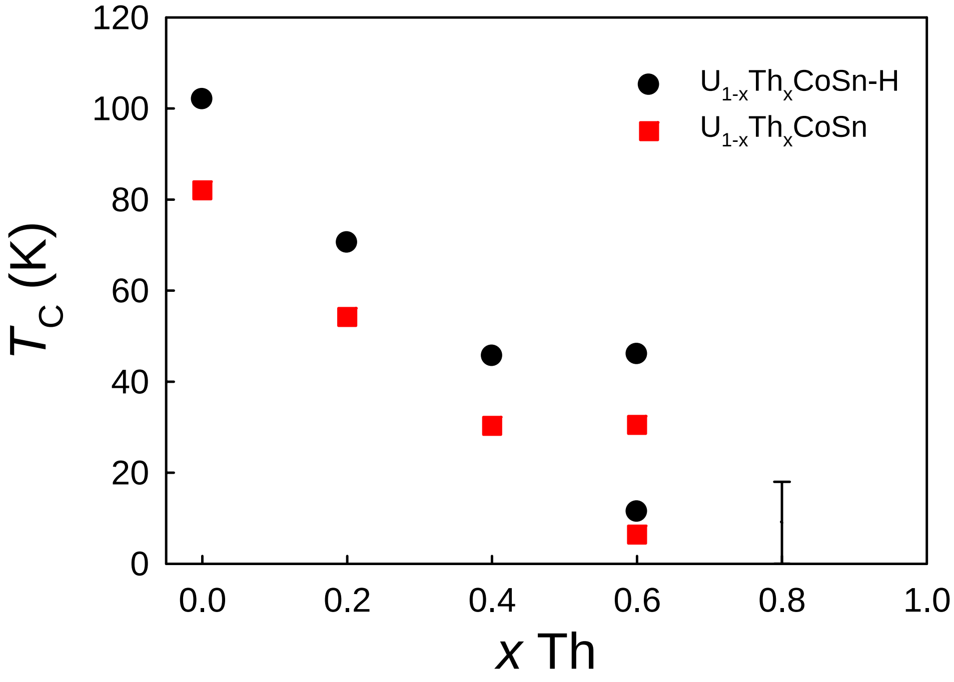

Fig. 30: Concentration dependence of Curie temperatures of $U_{1-x}Th_xCoSn$ and their hydrides.

From the Fig. 31 we can see that there is some ferromagnetic impurity in measured samples. The data was corrected (Fig. 32) to this impurity using following formula:

$$\chi_{corr} = \frac{\chi(B_2)\cdot B_2 - \chi(B_1)\cdot B_1}{B_2 - B_1} \tag{21}$$

where χ (B_1) is susceptibility in magnetic field B_1 (in our case B_1 = 3 T) and χ (B_2) is susceptibility in magnetic field B_2 (in our case B_2 = 6 T).

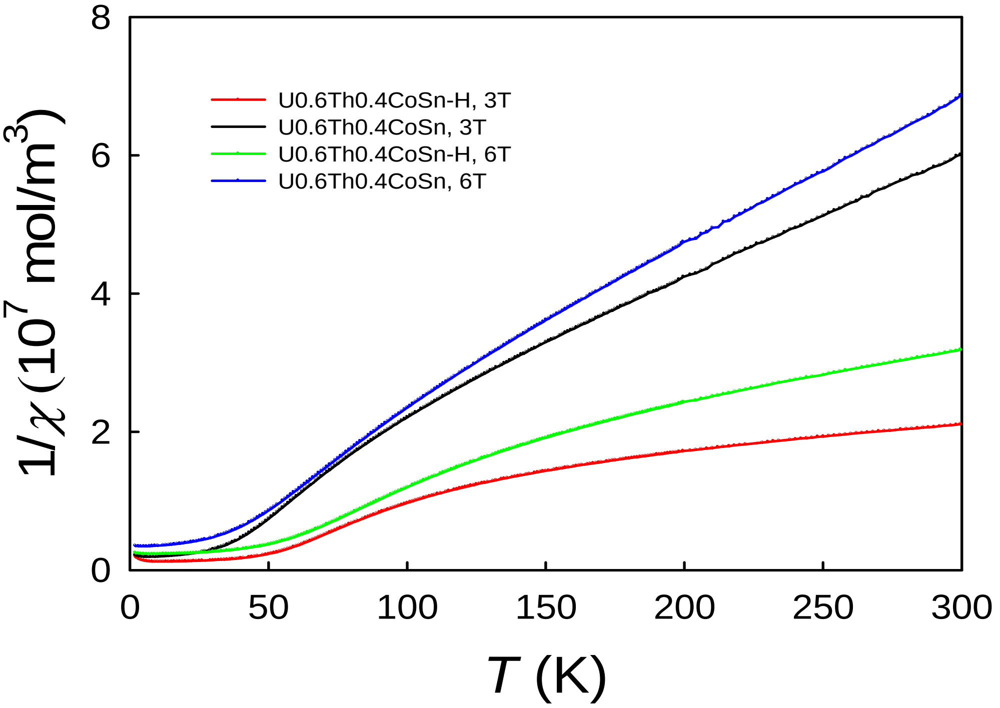

Fig. 31: Inverse susceptibility of $U_{0.6}Th_{0.4}CoSn$ and its hydride measured in 3 T and 6 T.

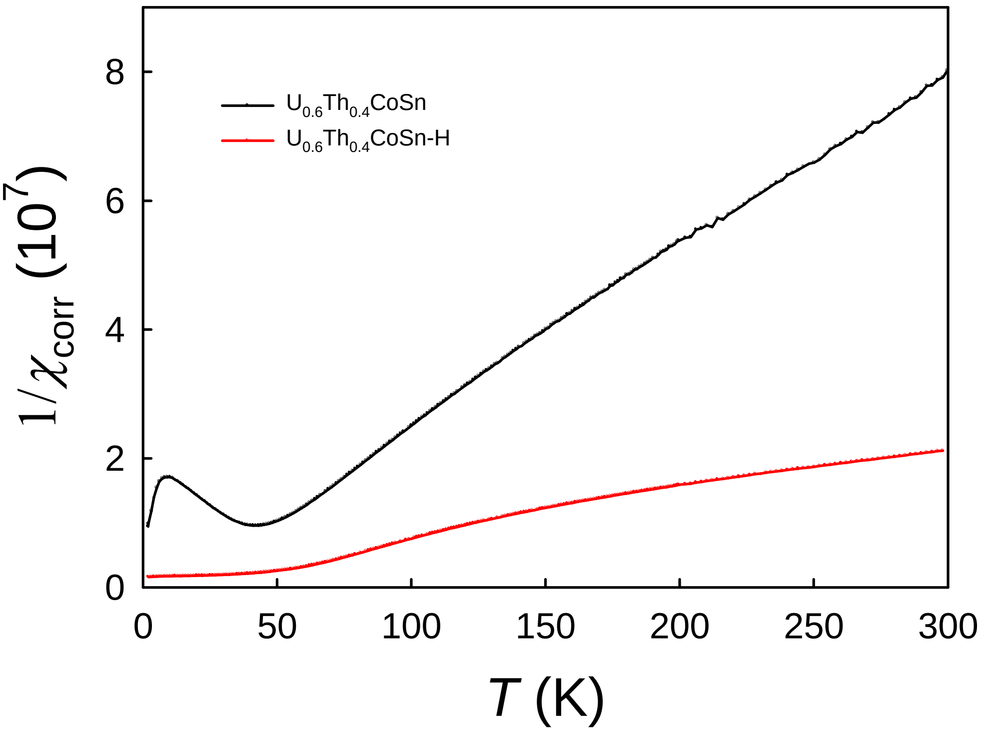

Fig. 32: Corrected susceptibilities of $U_{0.6}Th_{0.4}CoSn$ (black curve) and its hydrid (red curve).

URANIUM

All experiments on metal uranium were performed on polycrystalline sample on Quantum Design PPMS device at the Joint Laboratory for magnetic studies.

Magnetic measurement:

Magnetic susceptibility of uranium metal was measured in various temperatures. *M* (*B*) exhibits a small amount of ferromagnetic impurity developing with decreasing temperature. Slope d*M*/d*B* is constant; therefore the intrinsic susceptibility does not depend on *T*.

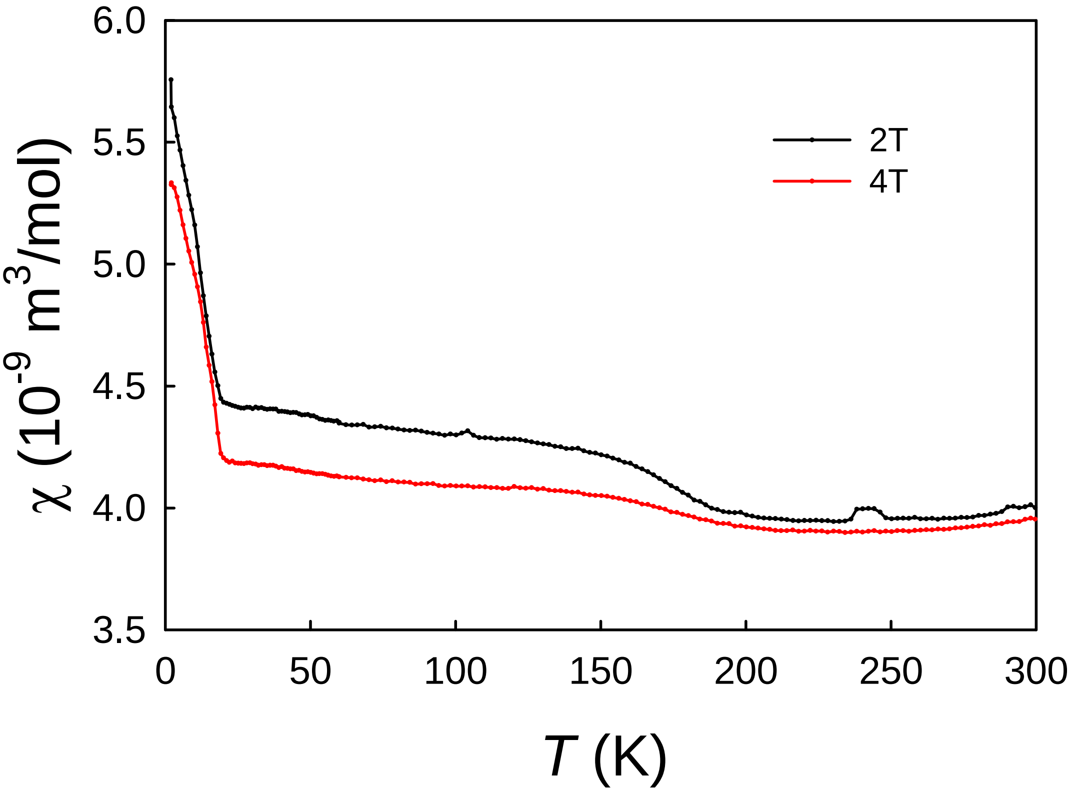

Fig. 33: Magnetic susceptibility of polycrystalline U-metal measured in various fields (red curve shown measurement in 4 T, black in 2 T).

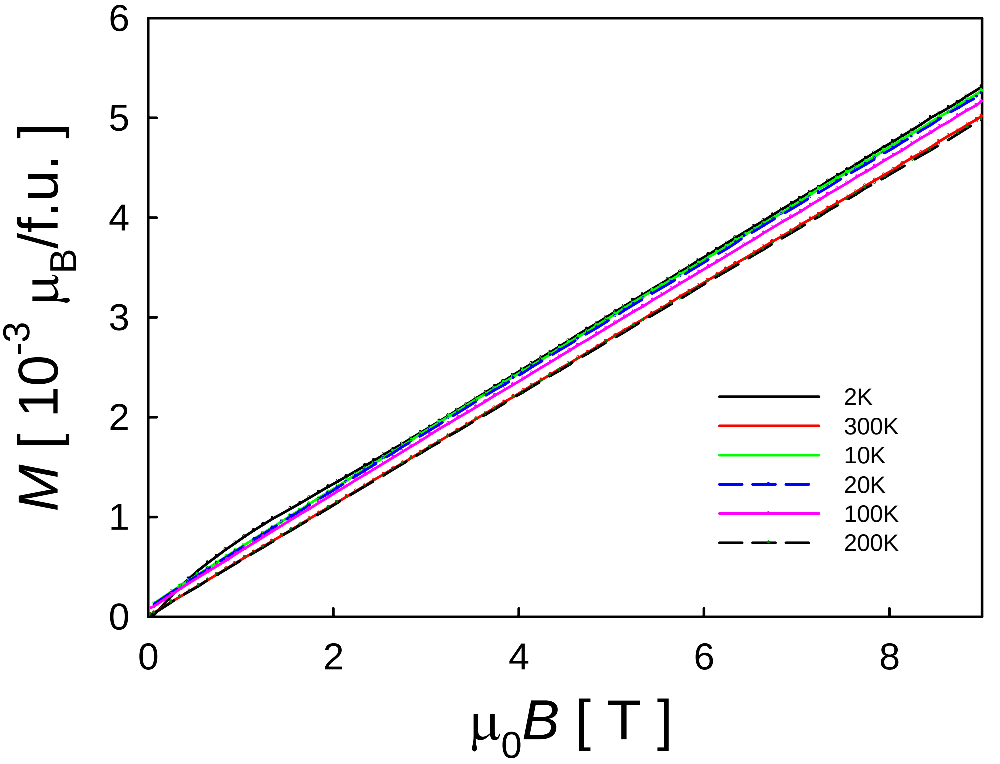

Fig. 34: Magnetization of polycrystalline U-metal measured in different temperatures.

Resistivity measurement:

The resistivity of the sample was measured in the temperature range from 2 K to 300 K on the polycrystalline sample. From the Fig. 35 we can see that there are no visible anomalies at the transition temperatures.

The low temperature data was fitted to $\rho = \rho_0 + aT^2$ to find the RRR ratio. The fitted curve was $\rho = 2.9642 \cdot 10^{-6} + 4.1672 \cdot 10^{-10} \cdot T^2$.

From that we calculated the RRR = 4.3182.

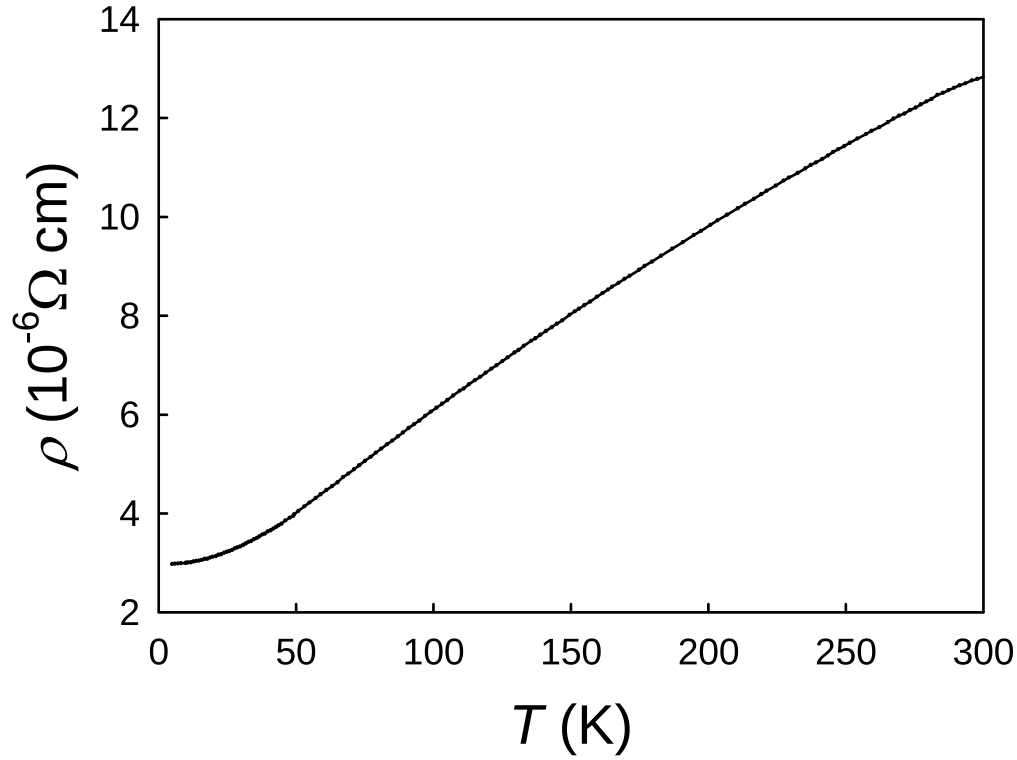

Fig. 35: The temperature dependence of the resistivity of uranium polycrystal.

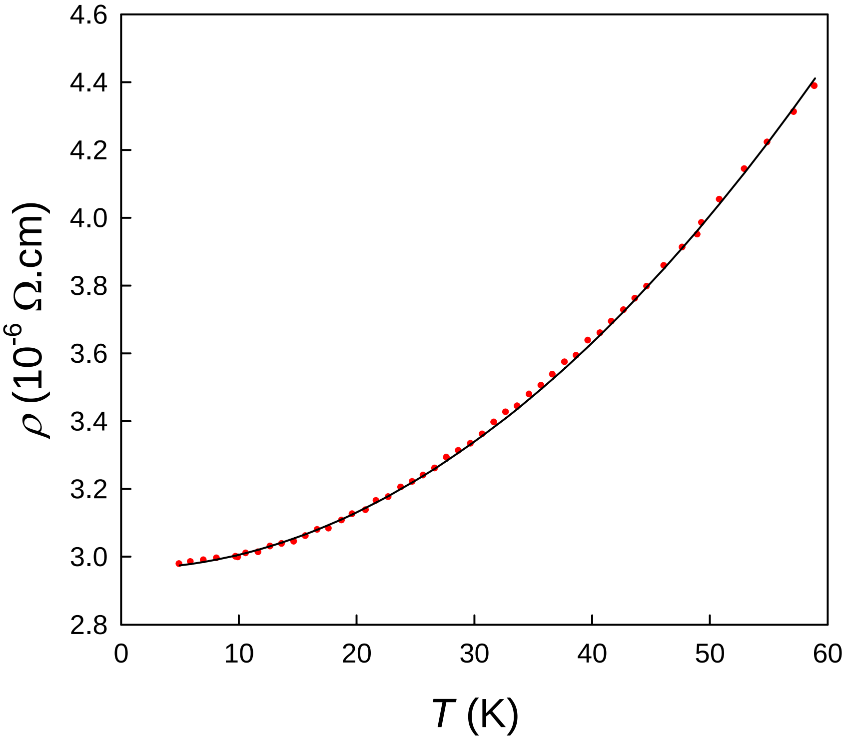

Fig. 36: Fitted resistivity of U-metal in low temperatures. Fitted to $\rho = \rho_0 + aT^2$

Specific heat measurement:

The heat capacity (specific) measurements were performed on polycrystalline sample using the PPMS measuring system in the temperature range 1.8-300 K. Here below (Fig.37) we show the comparison of our data with the data published by Lashley et al. [17]. The single crystal data from ref. 17 (black line) exhibit clear anomalies related to CDW transitions. The α_1 transition appears as a round hump in the specific heat data, the α_2 transition appears as a sharp peak and there is another broad peak at approximately 23 K (α_3 transition). On the polycrystalline samples there cannot be seen any peaks neither on published data nor on our data.

We can conclude that our data compare well with the data of Lashley on a polycrystal and do not show well-pronounced anomalies related to CDW transitions seen for single crystals. The presence of the CDW anomalies in specific heat can be therefore taken as possible indicator of the quality/crystallinity of U metal. This suggestion remains to be confirmed after the SSE refined U is available.

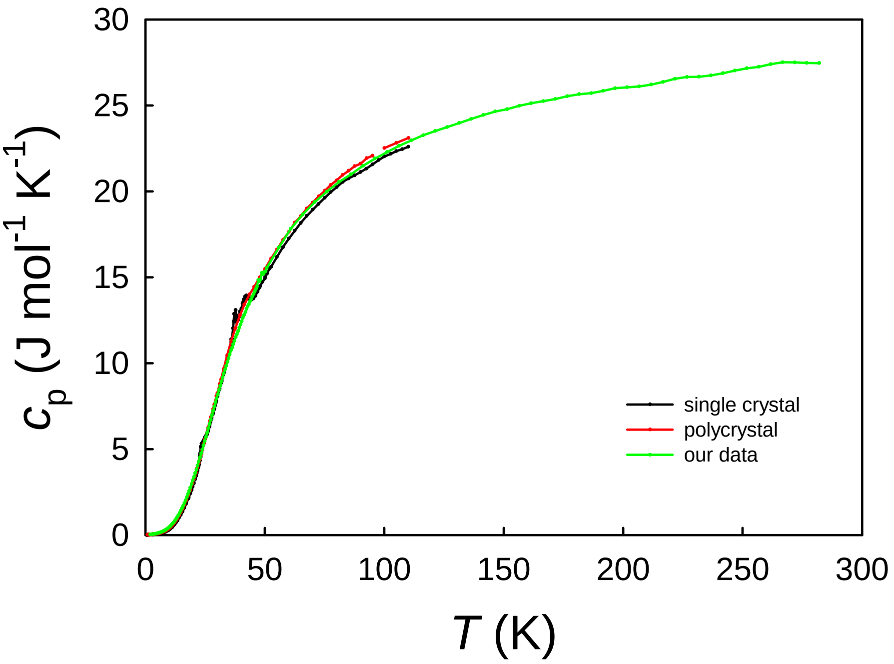

Fig. 37: Specific heat data. Black and red curves represent data obtained by Lashley at al. [17] (black curve was measured on single crystal, red curve on polycrystal). Green curve shows the data measured on our polycrystalline sample.

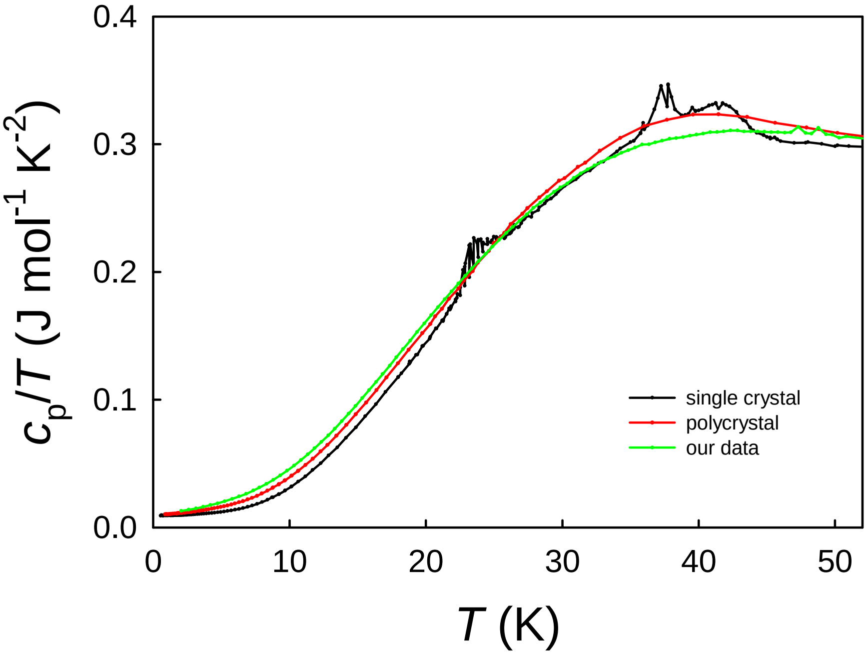

Fig. 38: c_p/T vs. T. Black and red curves represent data obtained by Lashley at al. [17] (black curve was measured on single crystal, red curve on polycrystal). Green curve shows the data measured on our polycrystalline sample.

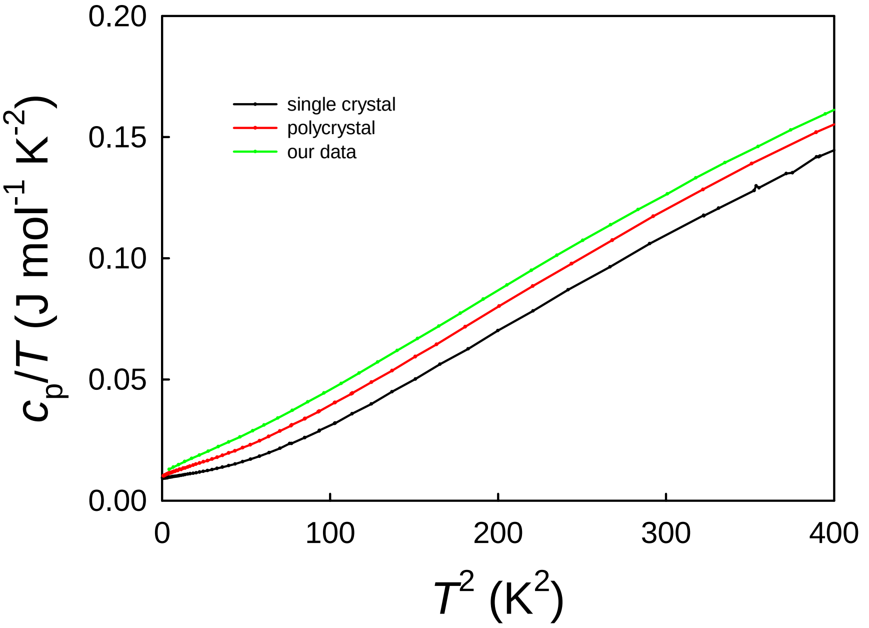

Fig. 39: c_p/T vs. T^2. Black and red curves represent data obtained by Lashley at al. [17] (black curve was measured on single crystal, red curve on polycrystal). Green curve shows the data measured on our polycrystalline sample.

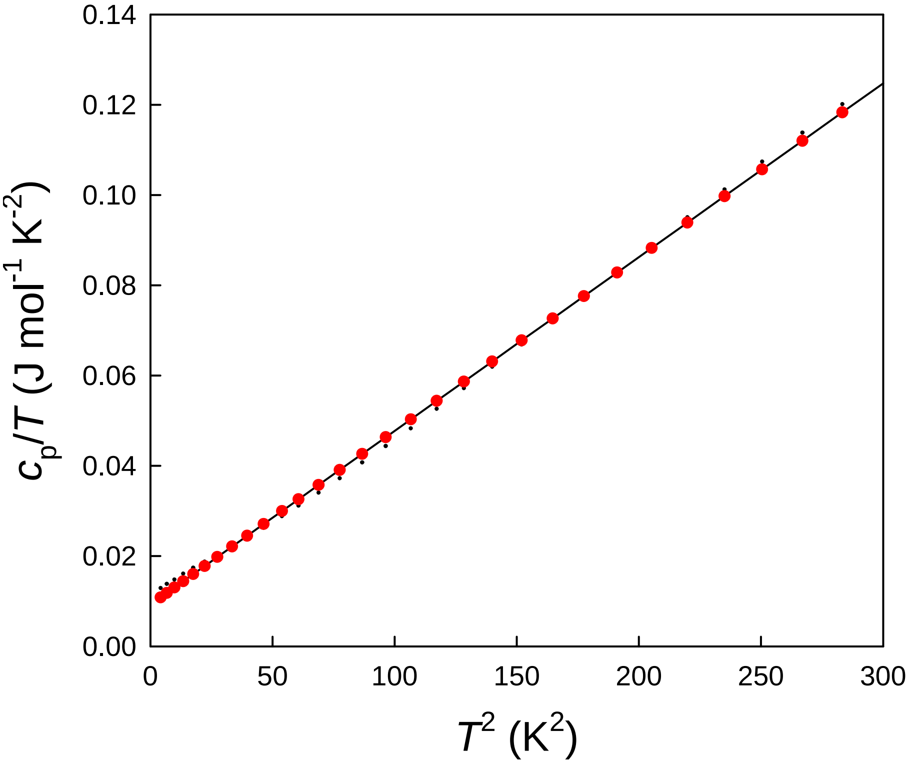

Fig. 40: Low temperature fit of specific heat of U-metal.

In addition, we determined the value of the Sommerfeld coefficient γ using the relation

$$c_\mathrm{p} = \gamma T + \beta T^3 , \tag{22}$$

known as a low temperature approximation for the Debye specific heat accounting for phonon cpecific heat term. We obtained the parameters $\gamma = 9.255\cdot10^{-3}$ J·mol^{-1}·K^{-2} and $\beta = 0.385 \cdot 10^{-3}$ J·mol^{-1}·K^{-4}.

Our value of specific heat $\gamma = 9.255\cdot10^{-3}$ J·mol^{-1}·K^{-2} is in a good agreement with the value $\gamma = 9.13\cdot10^{-3}$ J·mol^{-1}·K^{-2} obtained by Lashley et al. [17].

5. Conclusions

The crystal structures of $U_{1-x}Th_xCoSn$-H system were studied by X-ray powder diffraction (Cu-Kα radiation) and refined using a full-profile Rietveld analysis. We found that the structure type is not changed upon hydrogenation. It only leads to an expansion of unit cell, ranging between 3.0% and 3.6%. Both lattice parameters increase in the hydride, but the increment of c is increasing with increasing Th concentration while increment of a is reduced. More detailed X-ray analysis indicates that a phase separation occurs in the compounds with concentration 40 and 60 % of Th both in parent compounds and hydrides.

The stoichiometry of hydrides was determined by means of controlled thermal decomposition of hydrides in a closed volume. The amount of absorbed hydrogen decreases from 1.4 to 0.8 H/f.u. with increasing Th concentration.

Studies of the temperature dependence of magnetic susceptibility indicate a certain increase of T_C in the hydrides, but the Th concentration at which ferromagnetism vanishes remains practically unchanged. The net increase of T_C is generally understood as due to increase of the density of states at the Fermi level, resulting from the 5*f* band narrowing. This concept naturally does not work when comparing the ordering temperatures of UCoSn with the Th doped compounds, although the latter have expanded volume. The presence of the additional type of states (those originating from Th) does not allow to use a single-band model. Two Curie temperatures found from AC susceptibility indicate possible phase separation found by X-ray analysis.

We can conclude that the impact of lattice expansion on magnetism does not help to shift the critical concentration of the onset of magnetism – we expect a more prominent effect of lattice expansion in the concentrated system where the U-U spacing has a prominent role. One can imagine that in the diluted systems, the H absorption can tune the U-U spacing in rare remaining U-rich clusters. Otherwise it only separates more the U and Th atoms, reducing the 5*f* hybridization with Th electronic states.

6. References

[1] Stoner E.C., *Proc. R. Soc. A* 154 (1936) 656.

[2] Stoner E.C., *Proc. R. Soc. A* 165 (1938) 372.

[3] L. Havela, K. Miliyanchuk, A.V. Kolomiets, A.V. Andreev, L.C.J. Pereira and A.P. Gonçalves: Magnetic properties of hydrides of uranium ternary intermetallics, *Proceedings of the 2nd International Symposium on Hydrogen in Matter, Uppsala 2005, American Institute of Physics*.

[4] K. Miliyanchuk, L. Havela, A.V. Kolomiets, A.V. Andreev: Structure and magnetism of a new series of UTSn hydrides. *Journal of alloys and Compounds* 404-406 (2005), 165-168.

[5] Westlake D.G., *J. Less-Common Met.* 75 (1980) 177.

[6] Westlake D.G., *J. Less-Common Met.* 90 (1983) 251.

[7] Westlake D.G., *J. Less-Common Met.* 91 (1983) 1.

[8] Westlake D.G., *J. Less-Common Met.* 91 (1983) 275.

[9] Lundin C.E., Lynch F.E. and Magee C.B., *J. Less-Common Met.* 56 (1977) 19.

[10] Hjörvarsson B., Guo J.-H., Ahuja R., Ward R.C.C., Andersson G., Ericsson O., Wells M.R., Sathe C., Agui A., Butorin S.M. and Nordgren J., *J. Phys.: Cond. Mater* 11 (1999) L119.

[11] Shoemaker D.P. and Shoemaker C.B., *J. Less-Common Met.* 68 (1979) 43.

[12] Wang X.W. and Chen C.F., *Phys. Rev. B* 56 (1997) R7049.

[13] Mulford R.N.R., Ellinger F.H. and Zachariasen W.H., *J. Am. Chem. Soc.* 76 (1954) 297.

[14] Rundle R.E., *J. Am. Chem. Soc.* 69 (1947) 1719.

[15] Rundle R.E., *J. Am. Chem. Soc.* 73 (1951) 4172

[16] V. Sechovsky, L. Havela, G. Hilscher, N. Pillmayr, A. V. Andreev, P. A. Veenhuizen, F. R. de Boer: 5*f* magnetism in (U,Th)CoSn, *J. Appl. Phys* 63 (8), 14 April 1988

[17] J. C.Lashley, B. E. Lang, J. Boerio-Goates, B. F. Woodfield, G. M. Schmiedeshoff, E. C. Gay, C. C. McPheeters, D. J. Thoma, W. L. Hults, J. C. Cooley, R. J. Hanrehan, Jr., and J. L. Smith: Low-temperature specific heat and critical magnetic field of α-uranium single crystal, *Phys. Rev. B* 63, 2001.

[18] Rodrigues-Carvajal J., FullProf Suite, LLB (CEA-CNRS), 2001.

[19] Rietveld H.M., *J. Appl. Cryst.* 2 (1969) 65.